Accepted Manuscript

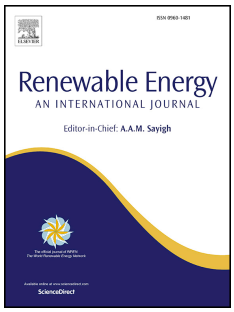

Power-to-load balancing for asymmetric heave wave energy converters with nonideal power take-off

Nathan M. Tom, Farshad Madhi, Ronald W. Yeung

PII: S0960-1481(17)31166-7

DOI: 10.1016/j.renene.2017.11.065

Reference: RENE 9467

To appear in: *Renewable Energy*

Received Date: 5 April 2017

Revised Date: 1 November 2017

Accepted Date: 22 November 2017

Please cite this article as: Tom NM, Madhi F, Yeung RW, Power-to-load balancing for asymmetric heave wave energy converters with nonideal power take-off, *Renewable Energy* (2018), doi: 10.1016/j.renene.2017.11.065.

Power-to-Load Balancing for Asymmetric Heave Wave Energy Converters with Nonideal Power Take-Off

Nathan M. Tom[a,*], Farshad Madhi[b,1], Ronald W. Yeung[b,2]

[a] *National Renewable Energy Laboratory, 15013 Denver West Parkway, Golden, CO, 80401*
[b] *University of California at Berkeley, Department of Mechanical Engineering, Berkeley, California, 94720*

Abstract

The aim of this paper is to maximize the power-to-load ratio for asymmetric heave wave energy converters. Linear hydrodynamic theory was used to calculate bounds of the expected time-averaged power (TAP) and corresponding surge-restraining force, pitch-restraining torque, and power take-off (PTO) control force with the assumption of sinusoidal displacement. This paper formulates an optimal control problem to handle an objective function with competing terms in an attempt to maximize power capture while minimizing structural and actuator loads in regular and irregular waves. Penalty weights are placed on the surge-restraining force, pitch-restraining torque, and PTO actuation force, thereby allowing the control focus to concentrate on either power absorption or load mitigation. The penalty weights are used to control peak structural and actuator loads that were found to curb the additional losses in power absorption associated with a nonideal PTO. Thus, in achieving these goals, a per-unit gain in TAP would not lead to a greater per-unit demand in structural strength, hence yielding a favorable benefit-to-cost ratio. Demonstrative results for "The Berkeley Wedge" in the form of output TAP, reactive TAP needed to drive WEC motion, and the amplitudes of the surge-restraining force, pitch-restraining torque, and PTO control force are shown.

Keywords: Asymmetric heave wave energy converter; power absorption control; structural load mitigation; nonideal PTO efficiency; "Berkeley Wedge"

1. Introduction

The Berkeley Wedge (TBW) [1, 2] is an asymmetric wave energy converter (WEC) that can also serve as a breakwater. It consists of an asymmetric floater, a power take-off (PTO) system, and a support structure. The particular shape of the floater, depicted in Fig. 1, was designed to experience minimal effects from viscosity in heave motion. The mounting structure limits the motion of the floater to heave only. The PTO system implemented in the design is a linear permanent-magnet generator (LPMG) [3]. When the damping of the LPMG is matched with the heave radiation damping of the floater at resonance, there will be almost no reflected or transmitted waves and almost all of the incident wave energy will be absorbed by the LPMG. TBW can be used nearshore to provide electricity for local communities and act as a breakwater (concurrently) to protect the harbor with very minimal environmental impact. It can also be attached to offshore structures and floating platforms to provide electricity and protect the structure. Additionally, TBW can be installed near the floating bridges to reduce the wave loads on the structure and generate electricity or desalinate seawater. In a recent study [4], the particular asymmetric shape of TBW was implemented in a coaxial wave energy converter (consisting of a fixed inner cylinder and moving outer cylinder) to reduce the viscous effects on the heave motion of the outer cylinder. The experimental testing revealed that the shape of TBW reduced the viscous damping on the heave displacement of the outer cylinder by 70%, resulting in an increase in the heave

*Corresponding author
Email addresses: nathan.tom@nrel.gov (Nathan M. Tom), madhi@berkeley.edu (Farshad Madhi), rwyeung@berkeley.edu (Ronald W. Yeung)
[1] Ph.D. Mechanical/Ocean Engineering, University of California at Berkeley
[2] Director, The Berkeley Marine Mechanics Laboratory, University of California at Berkeley

displacement of the outer cylinder by more than 300%.

The success of such or similar future WEC technologies will require the development of strategies to increase their survivability in extreme waves (survivability condition) and control strategies to adapt device performance to maximize energy generation while mitigating hydrodynamic loads to reduce the structural mass and overall cost in operational condition [5]. Regarding survivability of WECs, a recent study [6] presents a novel and practical solution to increase their survivability in extreme breaking waves. In this study, to reduce the effects of the extreme breaking waves on TBW while maintaining its operational draft, a novel solution of using pressure-relief channel, allowing water to flow through TBW, is presented and tested. Additionally, balancing the objectives of operational condition offers an interesting design and control challenge. For example, these are in contrast to previous works that solved the optimal control problem when focused solely on maximizing the time-averaged power (TAP). The application of state-constrained optimization [7, 8] to WEC control has gained significant traction recently as it provides the ability to include linear and nonlinear constraints. This optimization has been pursued using calculus of variations [7], model-predictive control [9–11], and pseudo-spectral methods [12–14]. If the PTO efficiency and structural loads are not considered, the optimum WEC trajectory follows that of complex conjugate control [15], which requires a substantial amount of reactive power when moving away from the resonance frequency. It is well known [16, 17] that the gains in power absorption when utilizing complex conjugate control can be counterbalanced by losses in the PTO accrued when reversing the energy flow to drive WEC motion and return energy to the wave system. It is possible that neglecting the conversion efficiency can lead to reduced or a net loss in the output power from the PTO resulting in a net flow of energy from the PTO to the WEC. Suboptimal strategies that eliminate reactive power, notably latching [18] and declutching [19], have been proposed, yet still do not include a load metric in the optimization. It can be expected that as the controller works to maximize the absorbed mechanical energy, the growth rate in structural loads may exceed the growth in TAP. To address this concern, this work incorporates the PTO control force and restraining loads in the objective function of the optimization routine. As a result, the optimizer must now balance the opposing contributions in an attempt to obtain the largest power-to-load ratio.

This paper begins by reviewing TBW device concept and hydrodynamic properties that allow it to be a perfect absorber. This is followed by constructing the heave time-domain equation of motion to provide the preliminaries for extension into its spectral representation. The PTO unit is expected to have a limit on the stroke length, which will have an effect on the maximum absorbed power; however, this work also considers the use of a nonideal PTO unit, with a conversion efficiency less than 100%, and will discuss how the efficiency and PTO force coefficients can be used to calculate the net power delivered to the grid. The upper and lower bounds on the output TAP, surge-restraining force, pitch-restraining torque, and PTO actuator force are calculated while assuming that the WEC motion was constrained but remains sinusoidal. The upper bound was calculated by solving for the PTO spring and damping coefficient pair that maximized the output power, not absorbed power, while the lower bound assumes that the non-ideal PTO system consists only of a linear-resistive damper, and in both cases the PTO force coefficients are constant and continuous throughout the wave cycle. Next, pseudo-spectral control (PSC) theory is reviewed followed by incorporating the surge-restraining force, pitch-restraining torque, and PTO actuator force into the optimization problem. Penalty weights are multiplied on the contributions to the objective function from the restraining and PTO loads to adapt the performance as desired. The effect of including the restraining loads on balancing power absorption and load shedding is first explored by varying the penalty weight magnitudes and comparing against the known performance bounds. The time history of WEC motion and PTO control force are presented to illustrate how per-unit increases in TAP can exceed the per-unit increase in restraining and PTO loads while having a minimal reactive power requirement. Finally, the analysis will be extended to irregular waves to study the fatigue loads on the TBW foundation and PTO.

2. The Berkeley Wedge

TBW shape was designed to experience the smallest effect from viscosity when encountering incident waves and in motion. The motion of the floater (shown in Fig. 1 with a cross-section constant over the entire width) is restricted to heave only. The physical dimensions of the asymmetric floater were chosen to fit the model testing facility at the University of California at Berkeley. A detailed theoretical and experimental study [1] confirmed the effectiveness of the design in reducing the viscous effect on the motion of the device, thereby capturing almost all of the incident wave energy and providing a calm water surface leeward of the asymmetric floater.

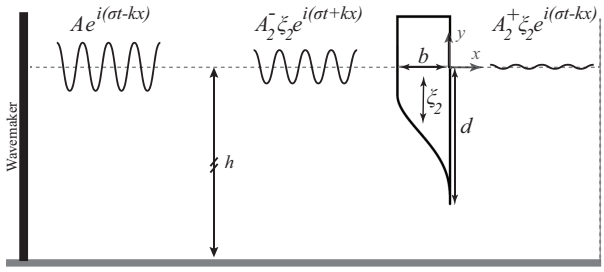

Figure 1: The schematics of the problem with specified incident and radiated waves.

In this study, the authors examined TBW with a draft, d, of 0.7 m and a beam, b of 0.212 m at the water plane. The particular shape of the front of the floater (Fig. 1) can be obtained from the following equation.

$$\mathscr{F}(\bar{y}) = 0.05926(\bar{y}+1)^2 + 3.88147(\bar{y}+1)^3 - 2.94074(\bar{y}+1)^4 \tag{1}$$

In Eq. (1), $\bar{x} = \mathscr{F}(\bar{y})$ is a shaping function, and $\bar{x} = x/b$ and $\bar{y} = y/d$ are nondimensional scales. In this equation, $\bar{y}$ can be shifted in height to obtain different drafts. The hydrodynamics coefficients for the asymmetric floater were obtained assuming a water depth, h, of 1.5 m while using the two-dimensional (2-D) potential-flow code RWYADMXA [20] and shown in nondimensional form in Fig. 2.

To analyze the optimal energy extraction efficiency of TBW, the relation between the heave wave-exciting force, heave-radiated damping, and the far-field radiated wave amplitude is discussed. Far-field radiated waves are generated as a result of heave displacement of the floater. They propagate away from the floater (Fig. 2(a)), facing the positive ($A_2^+\xi_2 e^{i(\sigma t-kx)}$) and negative ($A_2^-\xi_2 e^{i(\sigma t+kx)}$) x-coordinate. It can be shown that the heave wave-exciting force can be obtained from the far-field radiated wave amplitude in deep water by using the Haskind Relation (see Appendix C for the derivation).

$$X_2 = i\frac{\rho g^2}{\sigma^2}A_2^- \tag{2}$$

We can denote the geometry-hydrodynamic radiation factor, γ, to be the ratio of the left (A_2^-) and right (A_2^+) far-field radiated wave amplitudes.

$$\gamma = \left|\frac{A_2^+}{A_2^-}\right| \tag{3}$$

At this point, if we equate the work done by an oscillator on the fluid and the energy propagation associated with the far-field wave, we obtain the following expression (see Appendix C for details).

$$|X_2|^2 = \frac{2\rho g^2}{\sigma}\frac{\lambda_{22}}{1+\gamma^2} \tag{4}$$

With the above expression, we can obtain the optimal energy extraction efficiency for TBW, which will be discussed in later sections.

3. Time-Domain-Heave Equation of Motion

The one-degree-of-freedom time-domain-heave equation of motion is given by the following equation.

$$m\ddot{\zeta}_2(t) = f_{e2}(t) + f_{r22}(t) + f_h(t) + f_d(t) + f_m(t) \tag{5}$$

where t is time, m is the mass of the WEC, $\ddot{\zeta}_2$ is the heave acceleration, f_{e2} is the wave-exciting heave force caused by the incident waves, f_{r22} is the wave-radiation force caused by heave motion, f_h is the hydrostatic restoring force, f_d is

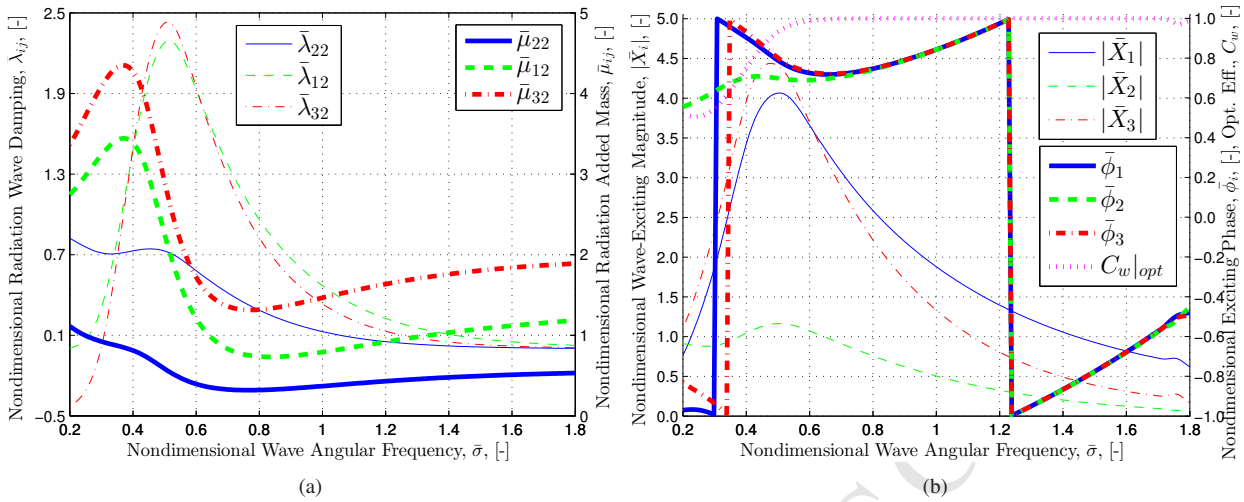

Figure 2: Nondimensional 2-D hydrodynamic radiation and wave-exciting coefficients. The nondimensional values are defined as: $\bar{\sigma} = \sigma\sqrt{b/g}$, $\bar{\mu}_{22} = \mu_{22}/\rho b^2$, $\bar{\lambda}_{22} = \lambda_{22}/\rho b^2\sigma$, $\bar{X}_2 = X_2/\rho g b$, $\bar{\phi}_2 = \phi_2/\pi$, $\bar{\mu}_{12} = \mu_{12}/\rho b^2$, $\bar{\lambda}_{12} = \lambda_{12}/\rho b^2$, $\bar{X}_1 = X_1/\rho g b$, $\bar{\phi}_1 = \phi_1/\pi$, $\bar{\mu}_{32} = \mu_{32}/\rho b^3$, $\bar{\lambda}_{32} = \lambda_{32}/\rho b^3\sigma$, $\bar{X}_3 = X_3/\rho g b^2$, $\bar{\phi}_3 = \phi_3/\pi$

the drag force caused by viscous effects, and f_m is the mechanical force applied by the PTO system.

The heave hydrostatic restoring force is given by the following equation.

$$f_h(t) = -C_{22}\zeta_2(t) \ , \quad \text{with} \ \ \mathrm{C}_{22} = \rho \mathrm{g} \mathrm{b} \tag{6}$$

where ρ is the fluid density, g is the gravitational acceleration, b is the device beam length at the calm water line, and ζ_2 is the time-varying heave displacement.

The linear hydrodynamic wave-radiation heave force will be represented in the time domain using the Cummins equation [21] and is written according to the following equation.

$$f_{r22}(t) = -\mu_{22}(\infty)\ddot{\zeta}_2(t) - \int_{-\infty}^{t} K_{r22}(t-\tau)\dot{\zeta}_2(\tau) \tag{7}$$

where $\mu_{22}(\infty)$ is the heave-added mass at infinite frequency, and K_{r22} is the heave radiation impulse response function, also known as the memory function because it represents the wave radiation memory effect caused by past WEC motions.

The wave-exciting heave force can be written in the time domain as follows.

$$f_{e2}(t) = \int_{-\infty}^{\infty} K_{e2}(t-\tau)\eta(\tau)\,d\tau \tag{8}$$

where K_{e2} is the heave wave-excitation kernel, which is noncausal, and η is the wave elevation.

The drag force can be represented by either of the following equations.

$$f_d(t) = \begin{cases} -\lambda_{vl}\dot{\zeta}_2(t) \\ -\lambda_{vn}\dot{\zeta}_2(t)\left|\dot{\zeta}_2(t)\right| \end{cases} \tag{9}$$

where λ_{vl} is the linear-drag coefficient caused by the presence of viscosity, and λ_{vn} is the quadratic-drag coefficient, assuming they are not negligible. The final one-degree-of-freedom heave equation of motion can now be shown in the following equation.

$$\begin{aligned}(m+\mu_{22}(\infty))\ddot{\zeta}_2(t) = &-C_{22}\zeta_2(t) - \lambda_{vl}\dot{\zeta}_2(t) \\ &- \int_{-\infty}^{t} K_{r22}(t-\tau)\dot{\zeta}_2(\tau)\,d\tau \\ &+ \int_{-\infty}^{\infty} K_{e2}(t-\tau)\eta(\tau)\,d\tau + f_m(t)\end{aligned} \tag{10}$$

where the linear form of the drag force has been used.

3.1. Time-Domain Solution in Regular Waves

It is common practice to begin analysis under regular wave excitation in which the incident wave elevation is described using the following equation.

$$\eta(x,t) = \Re\left\{-\frac{1}{g}\frac{\partial\phi_0}{\partial t}\bigg|_{z=h}\right\} = \Re\left\{Ae^{i(\sigma t-kx)}\right\} = A\cos(\sigma t - kx) \tag{11}$$

where ϕ_0 is the incident wave potential, A is the wave amplitude, σ is the wave angular frequency, k is the wave number, and $i = \sqrt{-1}$ is the imaginary unit. The time-harmonic heave response is modeled as follows.

$$\zeta_2(t) = \Re\left\{\xi_2 e^{i\sigma t}\right\} \tag{12}$$

where ξ_2 is the complex amplitude of heave displacement.

Under regular wave excitation, the radiation-convolution integral can be simplified to the following expression.

$$f_{r22}(t) = -\Re\left\{\left[-\sigma^2\mu_{22}(\sigma) + i\sigma\lambda_{22}\right]\xi_2 e^{i\sigma t}\right\} \tag{13}$$

The wave-excitation-convolution integral can be written according to the following equation.

$$f_{e2}(t) = \Re\left\{AX_2(\sigma)\,e^{i\sigma t}\right\} \tag{14}$$

For the time being, the mechanical force from the PTO system will be described by the following equation.

$$f_m(t) = -\Re\left\{\left(C_g + i\sigma B_g\right)\xi_2 e^{i\sigma t}\right\} \tag{15}$$

where C_g is the linear PTO-restoring coefficient and B_g is the PTO linear-damping coefficient. The frequency-domain expressions can be inserted into Eq. (10), leading to the heave displacement response amplitude operator as shown in the following equation.

$$\frac{\xi_2}{A} = \frac{X_2}{\left[C_g + C_{22} - \sigma^2(m+\mu_{22})\right] + i\sigma\left[\lambda_{22} + B_g\right]} \tag{16}$$

where λ_{vl} has been set to zero because results revealed in [1] saw minimal effects from viscosity.

3.1.1. PTO Absorbed Power

The TAP absorbed by the PTO can be calculated using the following equation.

$$\frac{P_T}{A^2} = \frac{1}{2}B_g\sigma^2\left|\frac{\xi_2}{A}\right|^2 \tag{17}$$

Equation (16) can be inserted into Eq. (17) to calculate the optimal PTO damping at each wave frequency. The optimal, unconstrained, time-averaged absorbed power and PTO damping for each wave frequency is given as follows.

$$\begin{aligned}\frac{P_T}{A^2} &= \frac{1}{4}\frac{|X_2|^2}{\lambda_{22}}\frac{1}{1+\sqrt{1+\left(\frac{C_{22}+C_g-\sigma^2(m+\mu_{22})}{\sigma\lambda_{22}}\right)^2}} \\ &= \frac{1}{2}\frac{\rho g^2}{\sigma}\frac{1}{1+\gamma^2}\frac{1}{1+\sqrt{1+\left(\frac{C_{22}+C_g-\sigma^2(m+\mu_{22})}{\sigma\lambda_{22}}\right)^2}} \end{aligned} \tag{18}$$

$$B_g = \lambda_{22}\sqrt{1+\left(\frac{C_{22}+C_g-\sigma^2\left(m+\mu_{22}\right)}{\sigma\lambda_{22}}\right)^2} \tag{19}$$

where at resonance $B_g = \lambda_{22}$, leading to the maximum time-averaged absorbed power [22]. Because these expressions do not consider motion constraints, it may be necessary to increase the PTO damping to remain under a given motion constraint. The required PTO damping is given as follows.

$$B_g = \left\{\left(\frac{A|X_2|}{\sigma|\xi_2|_{max}}\right)^2 - \left[\frac{C_{22}+C_g}{\sigma} - \sigma\left(m+\mu_{22}\right)\right]^2\right\}^{1/2} - \lambda_{22} \tag{20}$$

where $|\xi_2|_{max}$ is the maximum amplitude of heave displacement [23]. The instantaneous power absorbed by a power-take-off unit can be calculated as follows.

$$\begin{aligned}P(t) &= \frac{B_g|i\sigma\xi_2|^2}{2} \\ &+ \frac{1}{2}\left[|i\sigma\xi_2|^2|B_g - iC_g/\sigma|\cos\left(2\left(\omega t+\varphi\right)+\nu\right)\right] \end{aligned} \tag{21}$$

$$PA_{\pm} = 1 \pm \sqrt{1+\left(\frac{C_g}{\sigma B_g}\right)^2} \tag{22}$$

where φ is the phase angle of $i\sigma\xi_2$, ν is the phase angle of $B_g - iC_g/\sigma$, and $PA_{\pm}$ is the peak-to-average power ratio [23]. As seen in Eq. (21), if $C_g \neq 0$, the instantaneous power will fluctuate between negative and positive values, indicating a bi-directional energy flow. When there is no reactive power, $C_g = 0$, the peak-to-average power ratio is 2 and the instantaneous power oscillates between 0 and $2P_T$. The reactive component is eliminated at the resonance frequency of the isolated floating body and the peak-to-average power ratio is minimized at 2; however, when away from the resonant frequency, the peak-to-average power ratio quickly increases, resulting in large swings in the bidirectional energy flow. The time-averaged reactive power, defined as the power that the PTO returns to the oscillating body, can be calculated as follows.

$$P_R = \frac{1}{T}\int_0^T \min\left[P(t),\ 0\right]dt \tag{23}$$

To provide a measure of efficiency for a given device, the TAP contained within a propagating wave must be known. The time-averaged wave power per-unit width, P_w, can be obtained from the following equation.

$$P_w = \frac{\rho g A^2}{4}\sqrt{\frac{g}{k}\tanh kh}\quad\left[1+\frac{2kh}{\sinh kh}\right]\overset{kh\to\infty}{\approx}\frac{1}{8\pi}\rho g^2A^2T = \frac{1}{4}\frac{\rho g^2A^2}{\sigma} \tag{24}$$

where h is the water depth.

We denote C_w as the ratio of TAP absorbed by the PTO per the incident wave energy flux. Substituting the expression of heave wave-exciting force, Eq. (4), into the modulus of the expression for the heave-displacement response amplitude operator, Eq. (16), and using the maximum TAP condition, $B_g = \lambda_{22}$, the expression for optimal

energy extraction efficiency as a function of the geometry-hydrodynamics factor, γ, is obtained using the following equation.

$$C_w|_{\text{opt}} = \frac{1}{1+\gamma^2} \tag{25}$$

To obtain maximum extraction efficiency ($C_w = 1$), γ needs to be equal to zero. This is possible by having the right far-field radiated wave amplitude equal to zero ($A_j^+ = 0$) and the left far-field radiated wave amplitude be finite ($A_j^- \neq 0$). For symmetric floaters, both right and left far-field wave amplitudes will be equal ($A_j^- = A_j^+$), so $\gamma = 1$, which results in $C_w|_{\text{opt}} = 0.5$ if the maximum time-averaged absorbed power condition is satisfied. The graph of $C_w|_{\text{opt}}$ for TBW is shown in Fig. 2(b).

3.1.2. Maximum Time-Averaged Absorbed Power Under Constrained Motion

The maximum time-averaged absorbed power under motion constraints, while assuming sinusoidal motion, was explored in [24], which provides the following expression.

$$P_T = \begin{cases} \frac{1}{8}A^2|X_2|^2/\lambda_{22} & \delta > 1 \\ \frac{1}{2}A|X_2|\sigma|\xi_2|_{max} - \lambda_{22}\sigma^2|\xi_2|^2_{max} & \delta < 1 \end{cases} \tag{26}$$

$$\delta = \frac{\sigma|\xi_2|_{max}}{A}\frac{2\lambda_{22}}{|X_2|} \tag{27}$$

where δ is the ratio between the constrained-to-optimal heave velocity, which is set by $|\xi_2|_{max}$, the maximum heave displacement amplitude. The associated PTO linear-damping coefficients are given as follows.

$$B_g = \begin{cases} \lambda_{22} & \delta > 1 \\ \frac{A|X_2|}{\sigma|\xi_2|_{max}} - \lambda_{22} & \delta < 1 \end{cases} \tag{28}$$

$$C_g = -\left[C_{22} - \sigma^2(m + \mu_{22})\right] \tag{29}$$

where the PTO spring coefficient cancels the dynamic force contribution from the hydrostatic body-restoring coefficient, mass, and hydrodynamic added mass, which is the basis of complex conjugate control [15].

The capture width, defined as the ratio between the TAP absorbed by the PTO, P_T, and the incident wave power per-unit width, P_w, is a metric used to evaluate the absorption efficiency of the device. The incident wave power is proportional to the incident wave amplitude squared, see Eq. (24). For unconstrained motion, which may also correspond to a very small incident wave amplitude, the capture width will be invariant to the incident wave height; whereas for a strongly constrained motion, which may also correspond to a very large incident wave amplitude, the capture width will be inversely proportional to the incident wave height and become less efficient from the hydrodynamic perspective.

3.1.3. Nonideal PTO Units

As discussed in [16, 17, 25], reactive control requires a two-way energy flow between the oscillating body and an energy storage system that will have losses associated with the energy flux reversal process. Considering a nonideal PTO unit, the peaks in the PTO instantaneous output power (P_+) and reactive input power (P_-) are given as follows.

$$P_\pm = \begin{cases} \eta_m \frac{B_g|i\sigma\xi_2|^2}{2}\left[1 + \sqrt{1 + \left(\frac{C_g}{\sigma B_g}\right)^2}\right] \\ \\ \frac{1}{\eta_m}\frac{B_g|i\sigma\xi_2|^2}{2}\left[1 - \sqrt{1 + \left(\frac{C_g}{\sigma B_g}\right)^2}\right] \end{cases} \tag{30}$$

where η_m is the PTO mechanical-to-electrical efficiency. The effect on the time-averaged output power is more complex because of the time-varying integration. The results from performing the integration over time were performed

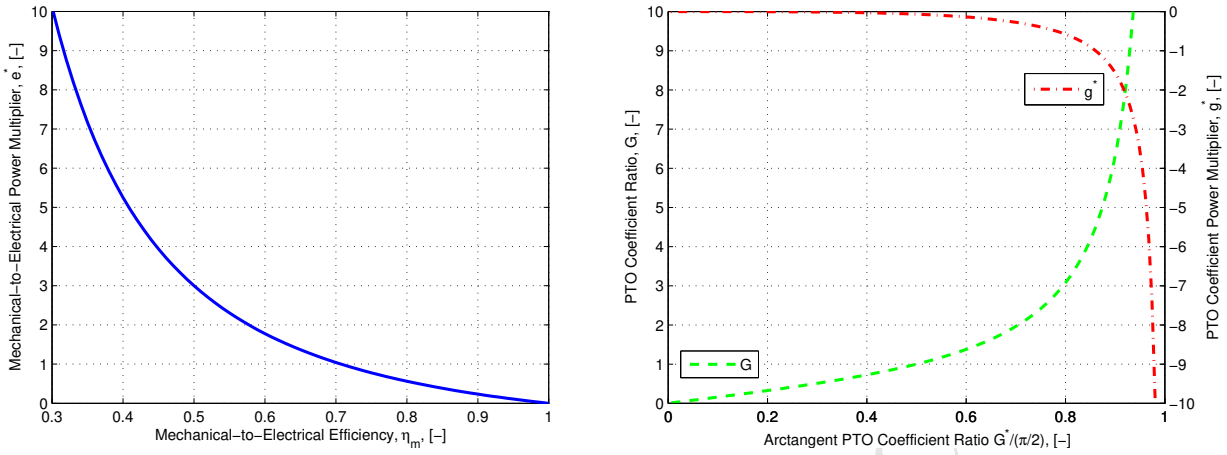

Figure 3: The effect on the mechanical-to-electrical efficiency power multiplier, e^*, the PTO coefficient power multiplier, g^*, and the PTO coefficient ratio, G, for a range of η_m and G^* values.

in [17, 25].

$$G = \left|\frac{C_g}{\sigma B_g}\right| \quad , \quad G^* = \arctan G$$
$$P_O = \eta_m \frac{B_g |i\sigma\xi_2|^2}{2} \left\{ 1 + \underbrace{\frac{1-\eta_m^2}{\eta_m^2}}_{e^*} \underbrace{\left(\frac{2G^* - \sin 2G^* - 2G\left(1-\cos^2 G^*\right)}{2\pi} \right)}_{g^*} \right\} \tag{31}$$

where P_O is the time-averaged power that is sent to the grid. The effect of G on e^* and g^* can be found in Fig. 3.

The nonideal PTO peak-to-average power (to the grid) ratios can now be calculated using the following equation.

$$PA_{\eta_m \pm} = \begin{cases} \dfrac{1+\sqrt{1+G^2}}{\left[1+\frac{1-\eta_m^2}{\eta_m^2}\left(\frac{2G^*-\sin 2G^*-2G\left(1-\cos^2 G^*\right)}{2\pi}\right)\right]} \\ \dfrac{1-\sqrt{1+G^2}}{\eta_m^2\left[1+\frac{1-\eta_m^2}{\eta_m^2}\left(\frac{2G^*-\sin 2G^*-2G\left(1-\cos^2 G^*\right)}{2\pi}\right)\right]} \end{cases} \tag{32}$$

3.2. Foundation Restraining Force and Torque

The structural foundation must handle the surge force and pitch torque needed to restrain the WEC to move only in heave. This will require a mounting structure to be designed to withstand the surge-restraining force and pitch-restraining torque which can be achieved using vertical guides that are driven into the seabed or mounted to an existing structure [1]. The restraining force in surge, X_{r1}, and restraining torque in pitch, X_{r3}, are given as follows.

$$A\left(X_{r1} + X_1\right) = \left[-\sigma^2\mu_{12} + i\sigma\lambda_{12}\right]\xi_2 \tag{33}$$
$$A\left(X_{r3} + X_3\right) = \left[-\sigma^2\left(x_g m + \mu_{32}\right) + i\sigma\lambda_{32}\right]\xi_2 \tag{34}$$

where X_1 and X_3 are the complex surge wave-exciting force and pitch wave-exciting torque coefficients per-unit wave amplitude, μ_{12} is the surge-heave added mass, and λ_{12} is the surge-heave wave radiation damping, μ_{32} is the pitch-heave added mass, λ_{32} is the pitch-heave wave radiation damping, and x_g is the horizontal center of gravity. The surge and pitch foundation reaction force and torque is affected by the radiation forces that result from the heave

motion of the WEC, which can be controlled by the PTO. The surge-restraining force and pitch-restraining torque can theoretically be eliminated if the complex heave displacement and PTO force amplitude satisfy the following equations.

$$\begin{aligned} \left.\frac{\xi_2}{A}\right|_{f_{r1z}} &= \frac{X_1}{-\sigma^2\mu_{12} + i\sigma\lambda_{12}} \\ \left.\frac{f_m}{A}\right|_{f_{r1z}} &= \left\{\left[C_{22} - \omega^2\left(m + \mu_{22}\right)\right] + i\sigma\lambda_{22}\right\}\left.\frac{\xi_2}{A}\right|_{f_{r1z}} - X_2 \end{aligned} \tag{35}$$

$$\begin{aligned} \left.\frac{\xi_2}{A}\right|_{f_{r3z}} &= \frac{X_3}{-\sigma^2\left(x_g m + \mu_{32}\right) + i\sigma\lambda_{32}} \\ \left.\frac{f_m}{A}\right|_{f_{r3z}} &= \left\{\left[C_{22} - \omega^2\left(m + \mu_{22}\right)\right] + i\sigma\lambda_{22}\right\}\left.\frac{\xi_2}{A}\right|_{f_{r3z}} - X_2 \end{aligned} \tag{36}$$

The time-domain corollary of Eqs. (33) and (34) is given as follows.

$$\begin{aligned} f_{r1}(t) = &-\int_{-\infty}^{\infty} K_{e1}(t-\tau)\,\eta(\tau)\,d\tau \\ &+ \mu_{12}(\infty)\,\ddot{\zeta}_2(t) + \int_{-\infty}^{t} K_{r12}(t-\tau)\,\dot{\zeta}_2(\tau)\,d\tau \end{aligned} \tag{37}$$

$$\begin{aligned} f_{r3}(t) = &-\int_{-\infty}^{\infty} K_{e3}(t-\tau)\,\eta(\tau)\,d\tau \\ &+ \left(x_g m + \mu_{32}(\infty)\right)\ddot{\zeta}_2(t) + \int_{-\infty}^{t} K_{r32}(t-\tau)\,\dot{\zeta}_2(\tau)\,d\tau \end{aligned} \tag{38}$$

3.3. Results from Fixed-PTO Coefficients

Maximizing the output TAP, as described in Sec. 3.1.3, involves the PTO coefficients to be fixed in time yet adapted for a given wave amplitude and angular frequency. Performance bounds can be set for the TAP, surge-restraining force amplitude, pitch-restraining torque amplitude, and PTO control force amplitude, which have been plotted in Fig. 4. A benefit of the current design can be observed in the bottom plot of Fig. 4(c), where the heave amplitude and phase required for elimination of the surge-restraining force and pitch-restraining torque are presented. The surge and pitch components require a very similar amplitude and phase for elimination, which will lead to a reduction in both if only one contribution is heavily penalized in the controller objective function. It is expected that time-varying PTO coefficients might be able to assist in optimizing the time-averaged absorbed power while reducing loads, leading to device performance that sits between the maximum constrained and passive curves.

4. Pseudo-Spectral Control (PSC)

The discretization of the control problem is completed by approximating the heave velocity and PTO force with a linear combination of basis functions [13, 26]. The heave velocity, $\dot{\zeta}_2$, and PTO mechanical force, f_m, are approximated by a zero-mean truncated Fourier series with N terms.

$$\dot{\zeta}_2(t) \approx \sum_{j=1}^{N/2} \psi_j^c \cos(j\sigma_0 t) + \psi_j^s \sin(j\sigma_0 t) = \Phi(t)\,\hat{\psi} \tag{39}$$

$$f_m(t) \approx \sum_{j=1}^{N/2} \tau_j^c \cos(j\sigma_0 t) + \tau_j^s \sin(j\sigma_0 t) = \Phi(t)\,\hat{\tau} \tag{40}$$

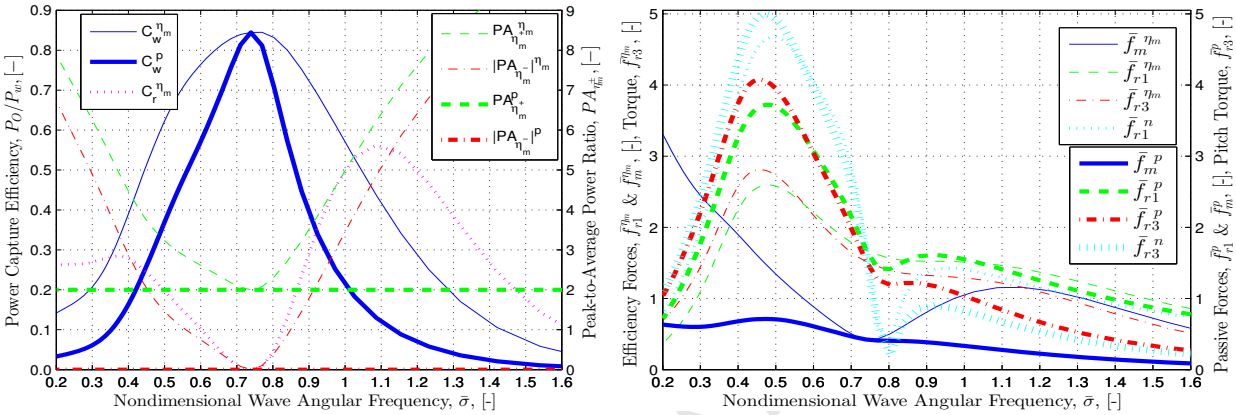

(a) Power Performance Metrics

(b) Load Performance Metrics

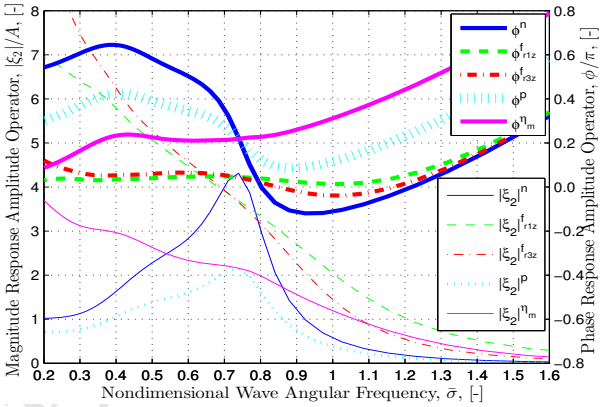

(c) Motion Performance Metrics

Figure 4: Performance bounds under a heave-displacement amplitude constraint of 0.1 m, a wave amplitude of 0.02 m, and a PTO efficiency of 85%. The superscript ^{p} denotes passive energy harvesting ($C_g = 0,\ B_g \geq 0$) and the superscript $^{\eta_m}$ denotes active energy harvesting ($C_g \neq 0,\ B_g \geq 0$) that maximizes Eq. (31). The superscript ^{n} denotes the natural heave motion ($C_g = B_g = 0$), whereas $^{f_{r1z}}$ and $^{f_{r3z}}$ denote the heave motion required to eliminate the surge-restraining force and pitch-restraining torque. The nondimensional force and torque values are given by: $\bar{f}_m = f_m/\rho g b A$, $\bar{f}_{r1} = f_{r1}/\rho g b A$, and $\bar{f}_{r3} = f_{r3}/\rho g b^2 A$.

where

$$\hat{\psi} = \left[\psi_1^c, \psi_1^s, \ldots, \psi_{\frac{N}{2}}^c, \psi_{\frac{N}{2}}^s\right]^\top, \ \hat{\tau} = \left[\tau_1^c, \tau_1^s, \ldots, \tau_{\frac{N}{2}}^c, \tau_{\frac{N}{2}}^s\right]^\top \tag{41}$$

$$\begin{aligned}\Phi(t) &= \left[\phi_1(t), \phi_2(t), \ldots, \phi_{N-1}(t), \phi_N(t)\right] \\ &= \left[\cos(\sigma_0 t), \sin(\sigma_0 t), \ldots, \cos\left(\frac{N}{2}\sigma_0 t\right), \sin\left(\frac{N}{2}\sigma_0 t\right)\right]\end{aligned} \tag{42}$$

with the fundamental frequency given by $\sigma_0 = 2\pi/T$ and T is the chosen time duration. The heave equation of motion can be described as follows.

$$M_{22}\hat{\psi} = \hat{\tau} + \hat{e}_2 \tag{43}$$

where $\hat{e}_2$ is the Fourier coefficient vector of the heave wave-exciting force. The matrix $M_{22} \in \mathbb{R}^{N\times N}$ is block diagonal with the following structure.

$$\begin{aligned}M_{22}^j &= \begin{bmatrix}\lambda_{22}(j\sigma_0) & \alpha(j\sigma_0) \\ -\alpha(j\sigma_0) & \lambda_{22}(j\sigma_0)\end{bmatrix} \ \text{for} \ \ j = 1, 2, \ldots, N/2 \\ \alpha(j\sigma_0) &= j\sigma_0\left(m + \mu_{22}(j\sigma_0)\right) - C_{22}/(j\sigma_0)\end{aligned} \tag{44}$$

The heave velocity coefficients can then be determined explicitly from the control and heave wave-exciting force Fourier coefficients. This representation allows the time-averaged absorbed energy, P_T, to be written as follows.

$$\begin{aligned}P_T &= \frac{1}{T}\int_0^T \dot{\zeta}_2(t) f_m(t)\, dt = \frac{1}{2}\hat{\psi}^\top\hat{\tau} \\ &= \frac{1}{2}\left[\hat{\tau}^\top\left(M_{22}^{-1}\right)^\top\hat{\tau} + \hat{e}_2^\top\left(M_{22}^{-1}\right)^\top\hat{\tau}\right]\end{aligned} \tag{45}$$

which is in the form of a traditional quadratic problem.

4.1. Penalty Terms

Penalty weights will be used in a mixed objective function to control the PTO force, surge-restraining force, and pitch-restraining torque.

4.1.1. Surge-Restraining Force

Load reduction will consist of limiting the forces on the WEC structure that are required to maintain the heave-only constraint. The surge-restraining force has two contributions that arise from the surge wave-exciting force and the radiation force that results from WEC heave motion. The equation for the surge-restraining force can be written in a matrix form, similar to Eq. (43), as follows.

$$\begin{aligned}\Phi(t)\hat{f}_{r1} &= -\Phi(t)\hat{e}_1 + \mu_{12}(\infty)\Gamma\hat{\psi} + \Phi(t)\left(G_{12} - \mu_{12}(\infty)\Gamma\right)\hat{\psi} \\ \hat{f}_{r1} &= -\hat{e}_1 + G_{12}\hat{\psi} = -\hat{e}_1 + G_{12}M_{22}^{-1}\hat{\tau} + G_{12}M_{22}^{-1}\hat{e}_2\end{aligned} \tag{46}$$

where $\hat{e}_1$ is the Fourier coefficients of the surge wave-exciting force, G_{12} and Γ are block matrices given in Appendix B and Eq. (43) has been substituted in the last expression. To maintain the convexity of the quadratic problem, the time-averaged squared ℓ^2-norm of the surge-restraining force vector was added to the objective function. The surge-restraining force penalty measure is given as follows.

$$\begin{aligned}\frac{\gamma_1}{T}|f_{r1}|^2 &= \frac{\gamma_1}{T}\int_0^T \hat{f}_{r1}^\top\Phi(t)^\top\Phi(t)\hat{f}_{r1}dt = \frac{\gamma_1}{2}\hat{f}_{r1}^\top\hat{f}_{r1} \\ &\approx \frac{\gamma_1}{2}\left(2\left[\hat{e}_1^\top G_{12}M_{22}^{-1} - \hat{e}_2^\top\left(M_{22}^{-1}\right)^\top G_{12}^\top G_{12}M_{22}^{-1}\right]\hat{\tau}\right. \\ &\quad \left. - \hat{\tau}^\top\left(M_{22}^{-1}\right)^\top G_{12}^\top G_{12}M_{22}^{-1}\hat{\tau}\right)\end{aligned} \tag{47}$$

where γ_1 is a penalty weight applied to the surge-restraining force. In the final expression for the surge-restraining force contribution, there are three constant terms independent of the PTO control force, which are left out of the optimization. See [14] for the full expression.

4.1.2. Pitch-Restraining Torque

Similar to the surge-restraining force, the pitch-restraining torque has two contributions that arise from the pitch wave-exciting torque and the radiation torque that results from WEC heave motion. As with the surge-restraining force, the time-averaged squared ℓ^2-norm of the pitch-restraining torque vector was added to the objective function. The pitch-restraining torque penalty measure is calculated as follows.

$$\frac{\gamma_3}{T}|f_{r3}|^2 \approx \frac{\gamma_3}{2}\left(2\left[\hat{e}_3^\top G_{32}M_{22}^{-1} - \hat{e}_2^\top\left(M_{22}^{-1}\right)^\top G_{32}^\top G_{32}M_{22}^{-1}\right]\hat{\tau} - \hat{\tau}^\top\left(M_{22}^{-1}\right)^\top G_{32}^\top G_{32}M_{22}^{-1}\hat{\tau}\right) \tag{48}$$

where $\hat{e}_3$ represents the Fourier coefficients of the pitch wave-exciting torque and γ_3 is a penalty weight applied to the pitch-restraining torque.

4.1.3. PTO Control Force

The PTO force is the only control actuation, and in an effort to reduce computational time and force spikes, a penalty weight was placed on the time-averaged squared ℓ^2-norm of the PTO force magnitude [9].

$$\frac{\beta_m}{T}|\tau_m|^2 = \frac{\beta_m}{T}\int_0^T \tau_m(t)\tau_m(t)dt = \frac{\beta_m}{2}\hat{\tau}^\top I_N\hat{\tau} \tag{49}$$

where β_m is a penalty weight associated with the control force magnitude and I_N is the identity matrix of size N.

4.2. Heave-Displacement Amplitude Constraint

Constraints on the heave-displacement amplitude reflect the physical limits of the system. These limits are modeled as inequality constraints.

$$\Phi(t)\,\Gamma^{-1}M_{22}^{-1}\hat{\tau} \le 1_{(N\times 1)}|\xi_2|_{max} - \Phi(t)\,\Gamma^{-1}M_{22}^{-1}\hat{e}_2\ , \tag{50}$$

$$-\Phi(t)\,\Gamma^{-1}M_{22}^{-1}\hat{\tau} \le -1_{(N\times 1)}|\xi_2|_{min} + \Phi(t)\,\Gamma^{-1}M_{22}^{-1}\hat{e}_2\ . \tag{51}$$

The constraints are enforced at specific time instants given by $t_k = kT/(N+1)$ for $k = 1, 2, \ldots N$ [26]. The constrained optimal control problem is now a convex quadratic program subject to linear constraints on the heave displacement amplitude. The impact of device motion and force constraints have been discussed in [27]; however, in this work no constraints were placed on the PTO control torque magnitude.

4.3. Final Objective Function

The objective function will be the sum of the time-averaged absorbed power, the squared ℓ^2-norm of the surge-restraining force, pitch-restraining torque, and PTO control force. The four contributions to the objective function are not of the same units, and the interrelationship between them is complex. Therefore, the final objective function will consist of the following nondimensional quantities.

$$J = \underbrace{\frac{P_T}{P_w}}_{C_w} + \gamma_1\left|\underbrace{\frac{f_{r1}}{\rho g b A}}_{\bar{f}_{r1}}\right|^2 + \beta_m\left|\underbrace{\frac{f_m}{\rho g b A}}_{\bar{f}_m}\right|^2 + \gamma_3\left|\underbrace{\frac{f_{r3}}{\rho g b^2 A}}_{\bar{f}_{r3}}\right|^2 \tag{52}$$

5. Pseudo-Spectral Results

For the regular wave simulations, the number of Fourier coefficients, N, was set to 100 while the fundamental frequency, σ_0, was set as the wave frequency, and the electrical-to-mechanical efficiency, η_m, was set at 85%.

5.1. Effect of Penalty Terms

Figure 5 verifies that the pseudo-spectral controller is achieving the desired results when considering the extremes of the tested penalty weights. As the control force penalty weight, β_m, is increased the magnitude of the PTO control force and reactive power is reduced. As shown for the lowest penalty weight values ($\gamma_1 \rightarrow 0$ and $\beta_m \rightarrow 0$), the highest TAP input to the PTO is achieved; however, the greatest TAP input may not correspond to the greatest output power when including nonideal efficiency ($\eta_m = 85\%$); see Fig. 5(b). In this range the surge-restraining force and pitch-restraining torque are slightly lower or equal to the values obtained when maximizing the WEC output power. This is a result of the amplification in heave displacement required to eliminate the restraining loads when the wave frequency does not coincide with the heave resonance frequency, refer to Fig. 4(c). However, the PTO control force and standard deviation in the output power are at minimum 10% greater when neglecting the PTO efficiency. Inclusion of the penalty weights in the optimization, not only reduce structural loads but are able to curb the additional power losses when utilizing a PTO unit with nonunity efficiency. For the largest values of γ_1 and β_m, reduction in the surge-restraining force and pitch-restraining torque, Fig. 5(c) and Fig. 5(d), is also followed by a corresponding decrease in the TAP. It is also possible to see an increase in the PTO force and reactive power requirement as emphasis is placed on reducing the surge-restraining force; see Fig. 5(e) and Fig. 5(f). The increase in PTO torque is a result of the amplitude and phase difference between the unforced (no PTO) and zero surge-restraining force heave motion; refer to Fig. 4(c). It can be observed that both above and below the resonance frequency the unforced heave amplitude of motion is lower than required for elimination of the surge-restraining force and pitch-restraining torque. As more emphasis is placed on reducing the surge-restraining force, the resulting increase in the PTO control force and reactive power imply that complete elimination of the restraining loads may not be desirable. These contour plots provide a clear design space that can be used to optimize power production, decrease structural loads, or achieve multiple combinations in between.

The left column of Fig. 5 plots a set of results for a wave frequency below resonance. In this frequency range the contours follow nearly straight lines when viewing the γ_1 and β_m space. As shown in Fig. 4(b), the lowest structural force and torque are obtained when maximizing for the output TAP, but this requires an increase in the PTO control force. The penalty weights in the objective function are linear constants multiplied to the surge-restraining force and pitch-restraining torque, therefore a reduction in structural loads is counteracted by a proportional increase in the PTO control torque, leading to contours that are predominantly straight lines. In the right column of Fig. 5, results are provided at a wave frequency above resonance, in which the constant value contours have greater curvature. In the high-frequency region, the lowest structural loads are observed when TBW oscillates naturally (no PTO). A reduction in restraint loads can first be achieved by decreasing the influence of the PTO control torque. This reduction can be observed by moving vertically along a constant β_m line; refer to Fig. 5(f). For example, by moving vertically along the $\beta_m = 1.0$, the PTO control torque will initially decrease, which also leads to a reduction in the restraint loads. However, eventually the PTO control torque 0.8 contour swings back across the $\beta_m = 1.0$ line, therefore the controller must now balance two load metrics that fight against one another.

5.2. Time History of WEC and PTO

Figure 6 plots the time history of the four points marked in the plots along the right column of Fig. 5. Near point 1, the maximum output power absorption is nearly recovered; near point 2, the surge-restraining force is prioritized at the expense of larger PTO forces and reactive power; near point 3, the controller attempts to maximize the output TAP with reduced PTO forces at the expense of larger restraint loads; and near point 4, there is roughly a 50%-60% reduction for all performance metrics compared to when the power output is maximized. As the penalty weights are reduced, the PTO control torque moves the heave velocity closer in phase with the heave wave-exciting force. This phase shift is accompanied by the greatest amplitudes in PTO control torque and pitch-restraining torque, but not for the reactive power. Marker 2 has the greatest reactive power requirement as the amplitude of motion required to eliminate the surge-restraining force is greater than the maximum power output heave profile. As the surge-restraining and PTO control force penalty weights are increased, the controller will first maintain a near optimum phase while reducing the amplitude of motion. However, eventually a greater phase shift is introduced by the controller to eliminate a larger proportion of the surge-foundation force that can be observed by comparing marker 2 and marker 4 in Fig. 6(a). Further reduction in the restraint loads will reveal an increase in the heave amplitude of motion and a corresponding increase in PTO control torque and reactive power. A larger reduction in restraint loads and PTO force, compared to the power output, can be achieved because of the ability of the controller to induce a phase shift in the heave velocity at the expense of bidirectional energy flow.

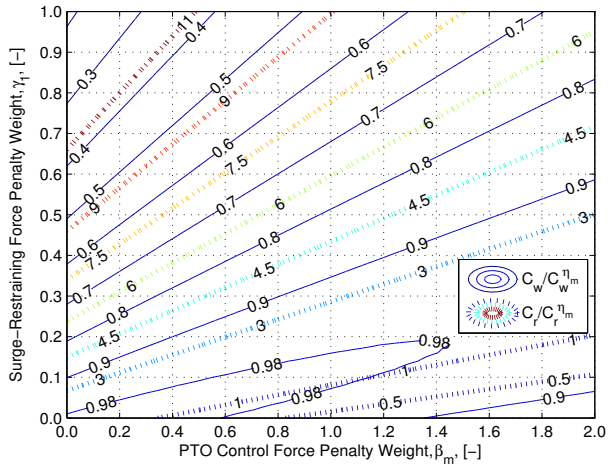

(a) Output, C_w, and Reactive Power, C_r, at $T = 1.5$ s

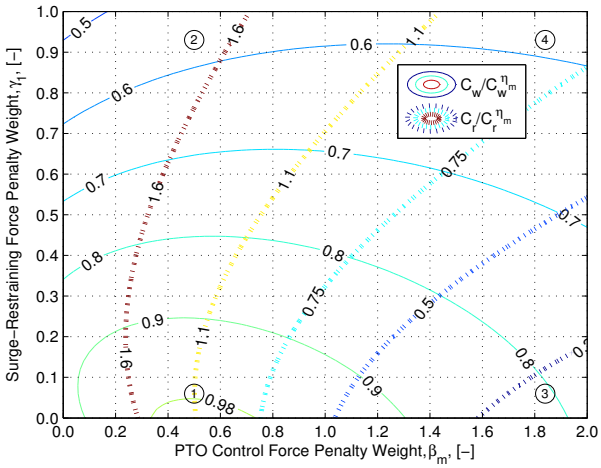

(b) Output, C_w, and Reactive Power, C_r, at $T = 1.0$ s

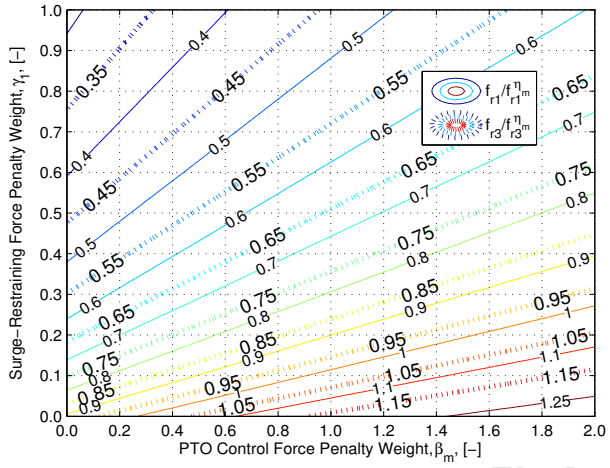

(c) Surge-, f_{r1}, and Pitch-Restraining Loads, f_{r3}, at $T = 1.5$ s

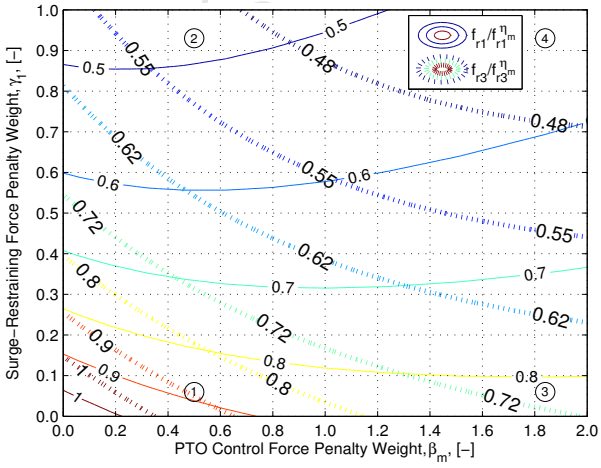

(d) Surge-, f_{r1}, and Pitch-Restraining, f_{r3}, Loads at $T = 1.0$ s

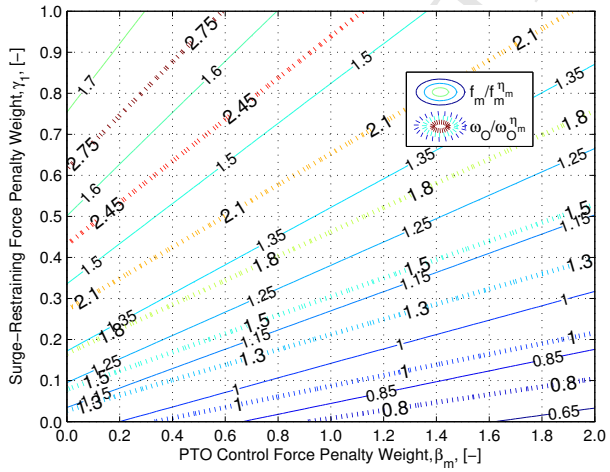

(e) PTO Force, f_m, and Power Variance, ω_O, at $T = 1.5$ s

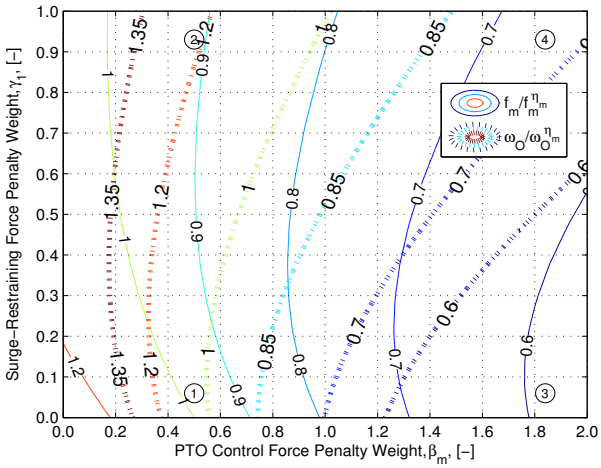

(f) PTO Force, f_m, and Power Variance, ω_O, at $T = 1.0$ s

Figure 5: Sensitivity of performance metrics to penalty weights under a heave-displacement amplitude constraint of 0.1 m and a wave amplitude of 0.02 m. The left column plots show the results for a wave period of 1.5 s ($\bar{\sigma} = 0.62$) and the right column plots show the results for a wave period of 1 s ($\bar{\sigma} = 0.92$). The superscript $^{\eta_m}$ denotes the resulting performance from selecting the C_g and $B_g \geq 0$ pair that maximizes Eq. (31). The variable ω_O is the standard deviation of the instantaneous power output.

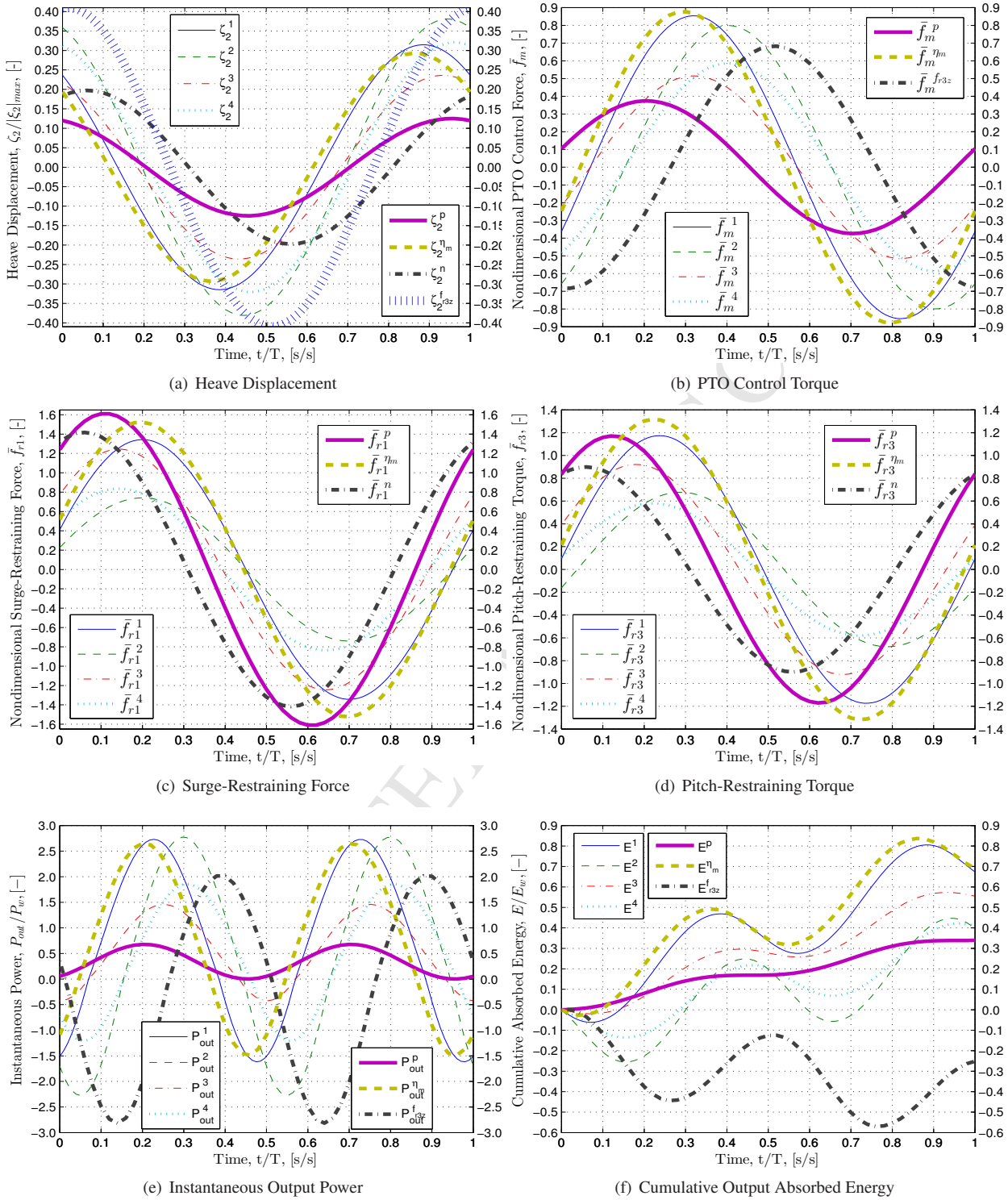

(a) Heave Displacement

(b) PTO Control Torque

(c) Surge-Restraining Force

(d) Pitch-Restraining Torque

(e) Instantaneous Output Power

(f) Cumulative Output Absorbed Energy

Figure 6: Time history of WEC motion, PTO control force, PTO power, surge-restraining force, and pitch-restraining torque. The pseudo-spectral control simulations were run with $T = 1$ s, $A = 2$ cm, a heave-displacement amplitude limit of 0.1 m, and varying penalty weights. The numeric superscripts 1, 2, 3, and 4 in the legend refer to the numeric markers in the right column of Fig. 5. The superscript $^{\eta_m}$ denotes the performance from selecting the C_g and $B_g \geq 0$ pair that maximizes Eq. (31). The superscript ^{p} denotes performance from setting $C_g = 0$ and selecting the $B_g \geq 0$ that maximizes Eq. (31). The superscript ^{n} denotes the natural heave motion ($C_g = B_g = 0$), whereas $^{f_{r3z}}$ denotes the heave motion required to eliminate the pitch-restraining torque. E_w is the cumulative absorbed energy when assuming perfect absorption.

5.3. Power-to-Load Ratio

To compare the results from PSC over a wider range of wave angular frequencies, a power-to-load ratio will be introduced as follows.

$$P_{tL} = C_w \left(\frac{C_w}{\bar{f}_{r1} + \bar{f}_m} \right) \left(\frac{P_O}{\omega_O} \right) \tag{53}$$

$$\chi = \frac{P_{tL}}{P_{tL}^{\eta_m}} \tag{54}$$

where ω_O is the standard deviation of the instantaneous output power. The first term in Eq. (53) represents the net output power to the grid that is directly related to the economics of operation; however, the second term is included to temper the controller from allowing large structural loads, leading to greater steel thickness and higher capital costs. The third term was introduced to limit the PTO peak instantaneous power and control actuation effort, thereby minimizing the PTO power capacity requirements. The value of $P_{tL}^{\eta_m}$ is obtained by inserting the performance values into Eq. (53) that result from using the PTO spring and damping coefficient pair that maximizes the output power from a nonideal PTO (refer to Eq. (31)). In a similar fashion, the value of P_{tL}^{p} is obtained by inserting the performance values into Eq. (53) that result from calculating the PTO damping coefficient ($C_g = 0$) that maximizes the output power of the nonideal PTO.

Ideally, it is desired that $\chi > 1$ as this provides the greatest power-to-load ratio. Several χ contours obtained from varying the combination of penalty weights γ_1 and β_m for the wave frequency of $\bar{\sigma} = 0.92$ are presented in Fig. 7(a). For penalty weight values in the space defined by $\gamma_1 < 0.4$ and $\beta_m > 0.6$, the contour values are favorable ($\chi > 1$). Next, for all the points along the contour $\chi = 1.6$, the surge-restraining force, pitch-restraining torque, PTO force, and energy capture were obtained and are plotted in Fig. 7(b). Although along the $\chi = 1.6$ contour the power-to-load ratio does not change, the absorbed energy and structural loads can vary. Additionally, the maximum χ contour for each wave frequency and penalty weight combinations were analyzed as shown in Fig. 7(c). A greater PTO power input requires frequencies lower than the resonance frequency to obtain the maximum power-to-load ratio.

To compare results across multiple wave frequencies, the maximum χ contours were calculated such that the enclosed areas were the same size but may differ in location in the γ_1 and β_m domain. The performance metrics along this χ contour were averaged for each frequency and the results are plotted in Fig. 8. It can be observed that the proposed PSC formulation is successful at providing power-to-load ratios that are equal to or greater than the baseline strategies with the largest values occurring about resonance; see Fig. 8(c). For the frequencies near resonance ($\bar{\sigma} = 0.74$), the power performance metrics for all strategies converge towards one another. This is to be expected—when oscillating at resonance, the spring and inertial terms cancel, which will not require a PTO spring coefficient to maximize energy absorption. However, it is interesting to see that PSC sacrifices a greater portion of power near resonance in return for greater reductions in the PTO torque and surge-restraining force; see Figs. 8(a) and 8(b). The greatest increase in the power-to-load ratio is observed at frequencies above resonance, whereas below resonance the power-to-load ratio from maximizing output power is nearly equivalent to PSC. The reason the power-to-load ratios are nearly equal is because below resonance the lowest restraining loads occur in conjunction with maximum output power (refer to Fig. 4), but requires the largest PTO force amplitude. The PSC optimizer concludes that further increase in power capture and reduction of the surge-restraining force and pitch-restraining torque is counteracted by the growth in PTO torque and the peak-to-average power ratios as shown in Fig. 8(d), which prohibits PSC from recovering the maximum power output.

6. Time-Domain Solution in Irregular Waves

The extension of psuedo-spectral control into the irregular wave environment will help evaluate the ability of the proposed control strategy to effectively reduce fatigue loads for both the WEC structure and PTO.

6.1. Wave Spectrum Characterization

The ocean water surface is exposed to variable winds and is typically very irregular. However, the surface can be considered as a superposition of multiple regular harmonic wave components. This linear superposition principle

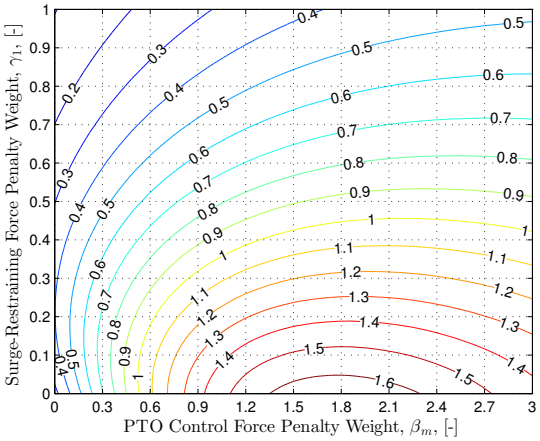

(a) Contour plot of χ

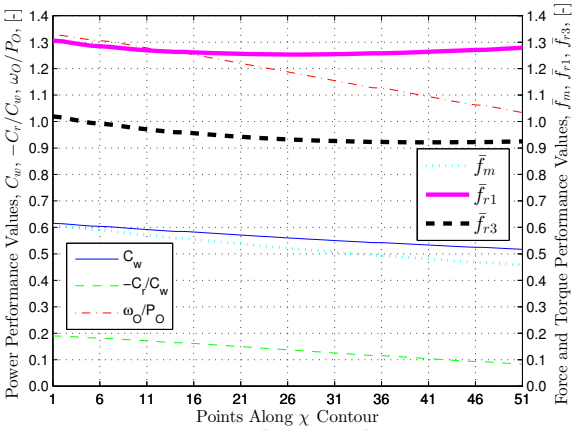

(b) Performance values for $\chi = 1.6$ in Fig. 7a

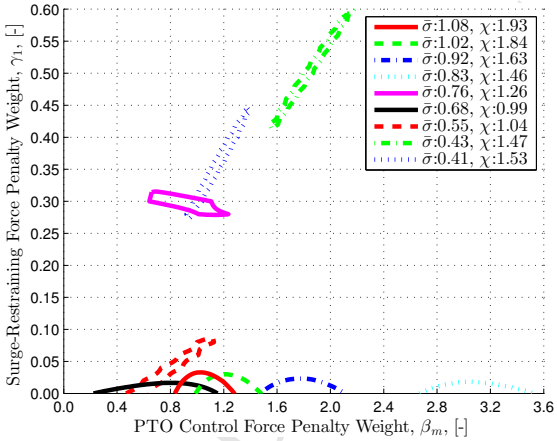

(c) Max χ contours for varying σ

Figure 7: Regular wave results for a wave amplitude of 0.02 m and wave period of 1.0 s ($\bar{\sigma} = 0.92$). The left plot consists of the constant χ contours as calculated from Eq. (54). The middle plot includes the variation in power and load performance values along the $\chi = 1.6$ contour in Fig. 7a. The right plot consists of the maximum χ values for a range of wave angular frequencies.

was first introduced in hydrodynamics by St. Denis and Pierson [28], which allows an irregular wave surface to be described as follows.

$$\eta(x,t) = \sum_{j=1}^{N} A_j \cos\left(\sigma_j t - k_j x + \varepsilon_j\right) \tag{55}$$

where N denotes the number of regular wave components used to describe the sea state and ε is a random phase angle between 0 and 2π. The wave number is related to the wave angular frequency through the dispersion relation. In this method the frequencies are chosen with a constant frequency step. As a result, the process will repeat after a time, T_r, given by $T_r = 2\pi/\Delta\sigma$ [29]. Unless surface elevation measurements are available, irregular seas are generally described by a wave spectrum. The wave spectrum is defined as follows.

$$S^+(\sigma)\, d\sigma = \frac{1}{2} A(\sigma)^2 \tag{56}$$

For a given a wave spectrum, the wave amplitude associated for a specific wave frequency is given as follows.

$$A(\sigma) = \sqrt{2 S^+(\sigma)\, d\sigma} \tag{57}$$

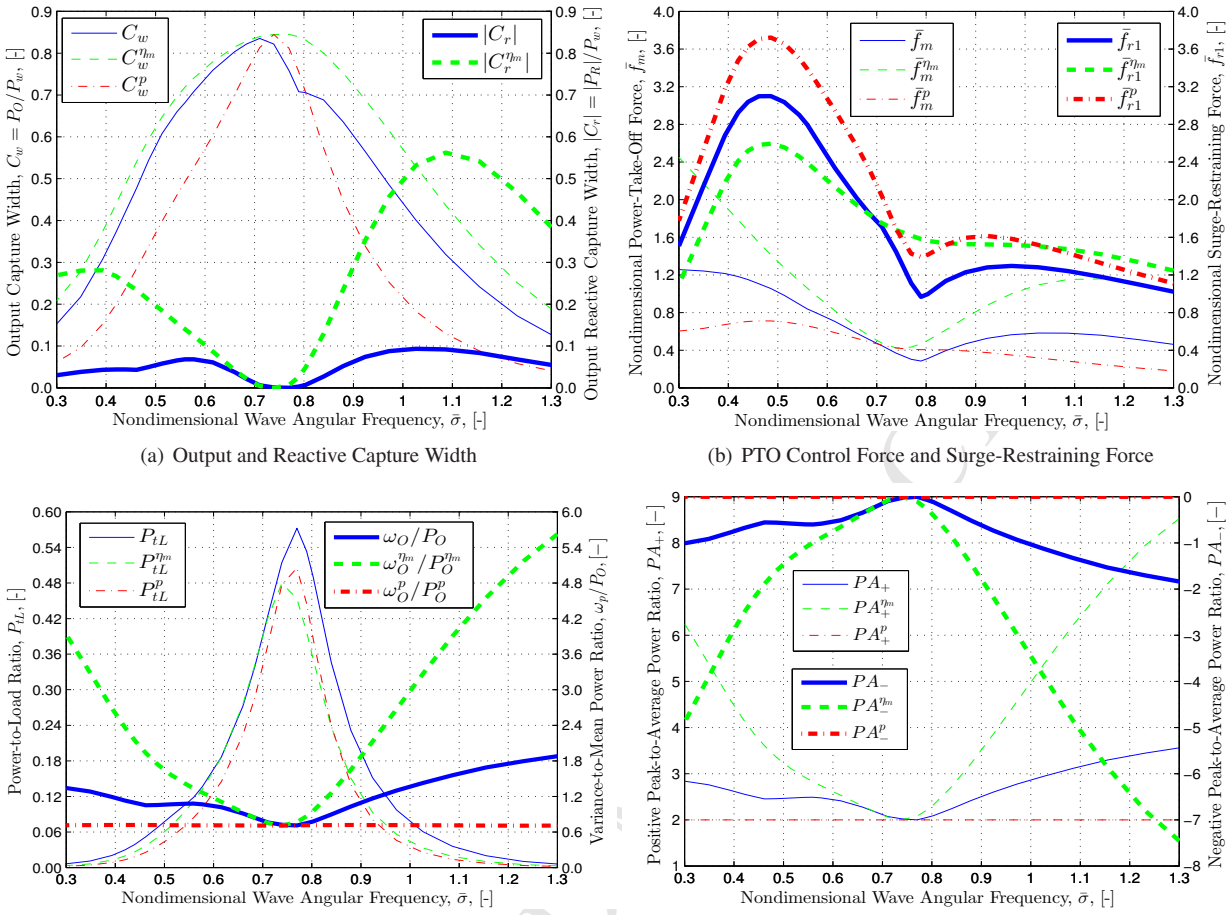

(a) Output and Reactive Capture Width

(b) PTO Control Force and Surge-Restraining Force

(c) Power-to-Load Ratio and Variance-to-Mean Power Ratio

(d) Positive and Negative Peak-to-Average Power Ratios

Figure 8: Regular wave results for a fixed wave amplitude of 0.02 m and varying wave period.

The Bretschneider spectrum [30] was chosen to apply PSC and is described by the following equation.

$$S^+(\sigma) = \frac{5}{16}\frac{\sigma_p^4}{\sigma^5}H_s^2 \exp\left[-\frac{5}{4}\left(\frac{\sigma_p}{\sigma}\right)^4\right] \tag{58}$$

where σ_p is the modal (peak) angular frequency of the wave spectrum and H_s is the significant wave height, traditionally defined as the mean wave height of the highest third of the waves. Relationships with the irregular wave statistics can be obtained by computing the spectral moments, m_n, of the wave spectrum.

$$m_n = \int_0^\infty \sigma^n S^+ d\sigma \tag{59}$$

The spectral moments can be used to calculate the following quantities of the irregular wave surface elevation.

$$H_s = 4\sqrt{m_0}\ , \quad H_a = \frac{5}{8}H_s, \quad \sigma_{-1} = \frac{m_0}{m_{-1}} \tag{60}$$

where H_s is the significant wave height, H_a is the average wave height, and σ_{-1} is the mean energy angular frequency.

The TAP available for a given irregular sea state is calculated using the following equation.

$$\begin{aligned} P_w &= \rho g \int_0^\infty V_g(\sigma) S^+(\sigma)\, d\sigma \\ &= \frac{\rho g}{2} \int_0^\infty \sqrt{\frac{g}{k}\tanh kh}\left[1 + \frac{2kh}{\sinh kh}\right] S^+(\sigma)\, d\sigma \\ &\overset{kh\to\infty}{\approx} \frac{1}{2}\rho g^2 m_0 \sigma_{-1} \end{aligned} \tag{61}$$

6.2. Pseudo-Spectral Optimal Control in Irregular Waves

Optimization of WEC performance in irregular waves requires a modification in calculating the Fourier coefficients of the heave wave-exciting force, surge wave-exciting force, and pitch wave-exciting torque. The surface elevation described by Eq. (55) will be used to calculate the heave wave-exciting force as follows.

$$\begin{aligned} f_{e2}(t) &= \Phi(t)\hat{e}_2 \\ &= \Sigma_{j=1}^{N/2} A(\sigma_j)\left[\Re\left\{X_2(\sigma_j)\right\}\cos\left(\sigma_j t + \varepsilon_j\right)\right. \\ &\left.-\Im\left\{X_2(\sigma_j)\right\}\sin\left(\sigma_j t + \varepsilon_j\right)\right] \\ &= \Sigma_{j=1}^{N/2} A(\sigma_j)\left[\left(\Re\left\{X_2(\sigma_j)\right\}\cos\varepsilon_j - \Im\left\{X_2(\sigma_j)\right\}\sin\varepsilon_j\right)\right. \\ &\left.\cos\sigma_j t - \left(\Re\left\{X_2(\sigma_j)\right\}\sin\varepsilon_j + \Im\left\{X_2(\sigma_j)\right\}\cos\varepsilon_j\right)\sin\sigma_j t\right] \end{aligned} \tag{62}$$

where the sum-difference trigonometric identities have been used in the second line. The above equation can be put in matrix form as follows.

$$\begin{aligned} \Phi(t)\hat{e}_2 = &\underbrace{\left[\cos\sigma_0 t,\ \sin\sigma_0 t,\ \ldots,\ \cos\frac{N}{2}\sigma_0 t,\ \sin\frac{N}{2}\sigma_0 t\right]}_{\Phi(t)} \\ &\underbrace{\begin{bmatrix} A(\sigma_0)\left(\Re\left\{X_2(\sigma_0)\right\}\cos\varepsilon_1 - \Im\left\{X_2(\sigma_0)\right\}\sin\varepsilon_1\right) \\ -A(\sigma_0)\left(\Re\left\{X_2(\sigma_0)\right\}\sin\varepsilon_1 + \Im\left\{X_2(\sigma_0)\right\}\cos\varepsilon_1\right) \\ \vdots \\ A(\frac{N}{2}\sigma_0)\left(\Re\left\{X_2(\frac{N}{2}\sigma_0)\right\}\cos\varepsilon_{N/2} - \Im\left\{X_2(\frac{N}{2}\sigma_0)\right\}\sin\varepsilon_{N/2}\right) \\ -A(\frac{N}{2}\sigma_0)\left(\Re\left\{X_2(\frac{N}{2}\sigma_0)\right\}\sin\varepsilon_{N/2} + \Im\left\{X_2(\frac{N}{2}\sigma_0)\right\}\cos\varepsilon_{N/2}\right) \end{bmatrix}}_{\hat{e}_2} \end{aligned} \tag{63}$$

which will have the same form for the surge wave-exciting force and pitch wave-exciting torque. The irregular wave-exciting Fourier coefficients can now be used in the controller routine; however, care must be taken in selecting σ_0 and N.

The nondimensionalization of the objective function for the irregular wave case will need to be adjusted because the incident wave elevation is time varying. Therefore, the force and torque penalty measures will be nondimensionalized by the average wave elevation as follows.

$$J = \frac{P_T}{P_w} + \gamma_1\left|\frac{f_{r1}}{\rho g b H_a/2}\right|^2 + \beta_m\left|\frac{f_m}{\rho g b H_a/2}\right|^2 + \gamma_3\left|\frac{f_{r3}}{\rho g b^2 H_a/2}\right|^2 \tag{64}$$

6.3. Fatigue and Equivalent Load Calculations

The inherent nature of irregular waves will lead to a variable-amplitude cyclic time series of forces and torques. In terms of fatigue, a variable-amplitude cyclic time series may be decomposed into individual load cycles using a rainflow cycle-counting algorithm [31], and it is assumed these individual cycles may be superimposed upon one another, according to Miner's Rule. For this analysis, the fatigue damage will be presented in terms of an equivalent

fatigue load, which is the constant-amplitude force or torque range that would, over the same number of cycles, cause an equivalent amount of damage as the original variable-amplitude stress time series [32]. The following definition will be used to calculate the equivalent load or torque.

$$f^{eq} = \left(\sum_{i=1}^{C} \frac{f^m}{C} \right)^{1/m} \tag{65}$$

where C is the cycle count and m is a material property normally defined as the slope of the logarithmic S-N fatigue curve. For this analysis, m will have a value of 3, which corresponds to fatigue properties of welded steel [33].

6.4. Irregular Wave Results

For the irregular wave simulations, the number of Fourier coefficients, N, was set at 180; the fundamental frequency, σ_0, was set at 0.1 rad/s; and the electrical-to-mechanical efficiency, η_m, was set at 85%. The power-to-load ratio used to evaluate PSC performance in irregular waves will be adjusted to account for the variable-amplitude force and torque time series as follows.

$$\begin{aligned} P_{tL} =& C_w \left(\frac{C_w}{f^*_{r1} + f^*_m} \right) \left(\frac{P_O}{\omega_O} \right) \ , \\ \chi = \frac{P_{tL}}{P_{tL}^{\eta_m}} \ , \ f^*_{r1} =& \frac{f^{eq}_{r1}}{\rho g b H_a/2} \ , \ f^*_m = \frac{f^{eq}_m}{\rho g b H_a/2} \end{aligned} \tag{66}$$

In the regular waves analysis, results were presented in terms of peak forces and loads because of the harmonic nature of the waves. On the other hand, in irregular waves, peak power and peak loads is sea-state-dependent and can be susceptible to the selection of the random phase angle ε. Thus, it was decided to use the standard deviation per TAP and fatigue-equivalent loads in the power-to-load calculations. The PSC power-to-load ratios, for a range of peak wave frequencies is on average 50% higher than other methods as shown in Fig. 9(c). The location of the maximum χ contours in the γ_1, β_m domain for each peak frequency are shown in Fig. 9(d). These χ contours are clustered in the region bounded by $\gamma_1 < 0.06$ and $0.3 < \beta_m < 1.6$, which has significantly less spreading compared to the regular wave simulations; refer to Fig. 7(c). Tighter clustering of the χ contours is a result of the energy contained within the sea state being spread across a larger number of wave frequencies. PSC must now account for a greater number of components of varying amplitudes and frequencies when optimizing the objective function. Thus, the influence of the wave frequencies above and below the peak frequency will have a greater influence on performance, resulting in greater overlap in penalty weights that generate the greatest power-to-load ratios.

In contrast to the irregular wave case, PSC produces the greatest output TAP compared to the baseline strategies; however, PSC has the largest reactive power requirement even when the peak period coincides with the resonance period, as shown in Fig. 9(a). This is another consequence of the spreading of wave energy, which PSC is able to exploit compared to the passive and active PTO efficiency-conscious baseline cases. The baseline cases solve for the set of PTO coefficients that maximize the output power, but remain constant over the duration of the simulation [34]. These baseline cases will not be as efficient at extracting the wave power at frequencies away from the peak period, but do not require future wave forecasting. The larger reactive power requirement also increases the variance in instantaneous power, but allows PSC to limit the fatigue-equivalent loads; see Fig. 9(b). In fact, the surge-restraining-force-equivalent loads obtained from PSC are the smallest for most of the simulated peak wave frequencies. The PTO control torque is largest for PSC when the peak wave frequency is near the resonant frequency; however, at the lower and higher wave frequencies, the PSC PTO torque fatigue load is surpassed by the active PTO efficiency-conscious baseline strategy. In these ranges, the optimizer will shed more of the available wave power as increasing the energy capture will be counteracted by greater growth in the PTO and structural loads.

7. Conclusion

In this paper, pseudo-spectral optimal control was used to balance power absorption against structural loading for a novel WEC and breakwater, The Berkeley Wedge. The analysis revealed that the power capture efficiency increased

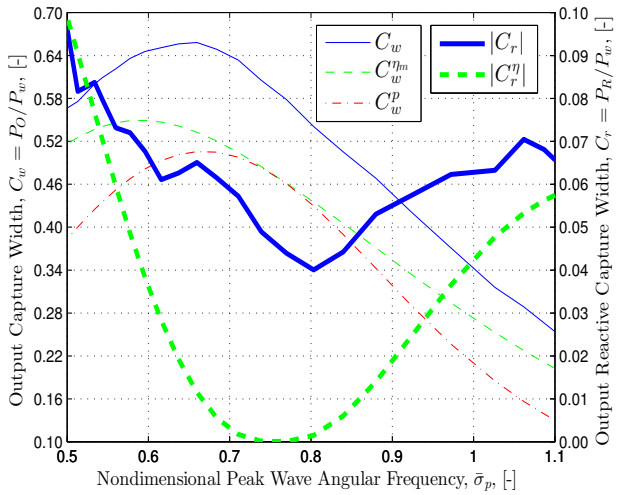

(a) Output and Reactive Capture Width

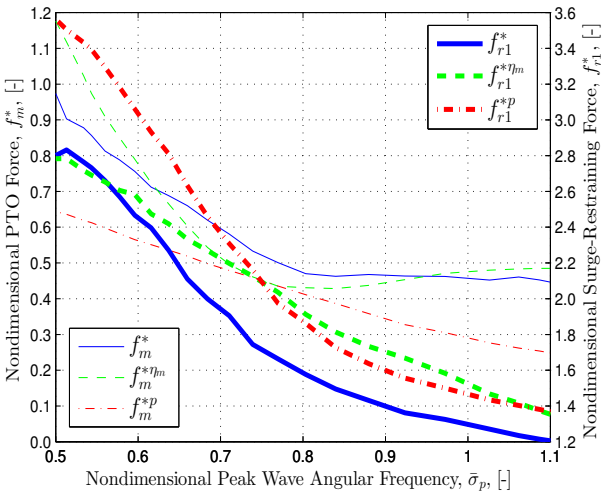

(b) PTO Control Force and Surge-Restraining Force

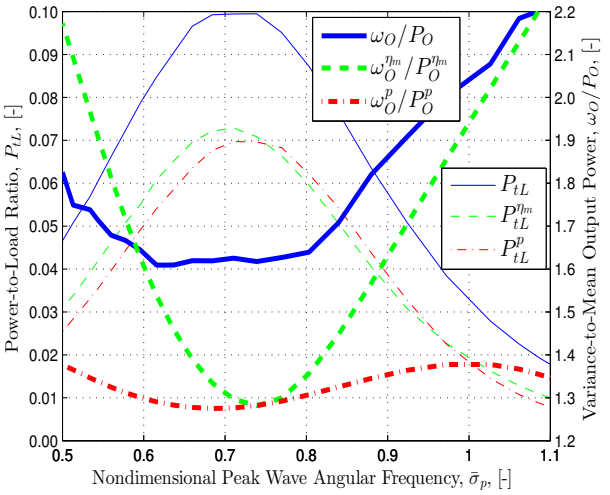

(c) Power-to-Load Ratio and Variance-to-Mean Power Ratio

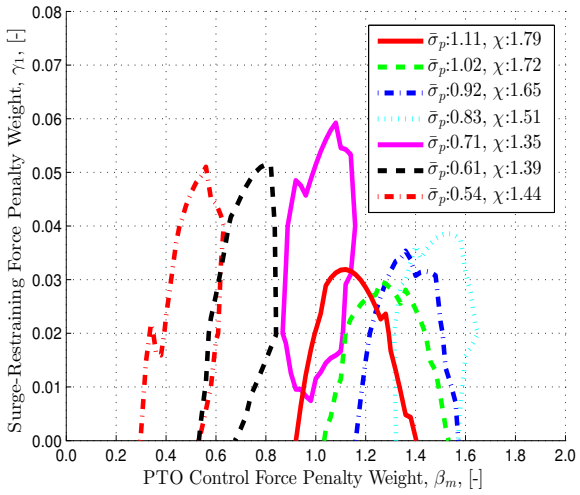

(d) Maximum χ Contours for Varying $\bar{\sigma}_p$

Figure 9: Irregular wave results for a fixed significant wave height of 0.1 m and varying peak period.

by more than 50% for lower and higher wave frequencies ($\bar{\sigma} < 0.6$ and $\bar{\sigma} > 0.8$), compared to results obtained from a passive PTO with a constant linear damper. However, as the wave frequency moves away from resonance, a greater reactive power component is required to achieve the highest power-to-load ratio. It was observed that for wave frequencies below resonance, the surge-restraining force and pitch-restraining torque are significantly lower, in the range of $\bar{\sigma} \leq 0.7$, when maximizing the PTO output TAP. Thus, when operating below the resonance frequency, achieving the most favorable power-to-load ratios requires the use of a PTO unit that allows for bidirectional energy flow. The magnitude of heave motion required to cancel the surge-restraining force and pitch-restraining torque were shown to generally be larger than the natural body motion. As a result, a significant increase in the PTO control force and reactive power may be required to eliminate the restraining loads.

The pseudo-spectral optimal control problem was extended by including the squared ℓ^2-norm of the surge-restraining force, pitch-restraining torque, and PTO actuator force to create a multiterm objective function. The optimizer performance was found to be adjustable based on the values chosen for each separate penalty weight placed on the three load contributions. In addition, the penalty weights used in the objective function were observed to be successful at representing the additional losses accrued with a PTO that has a non-unity efficiency. It was discovered that because

of the WEC hydrodynamics, increasing the penalty weight associated with either the surge-restraining force or pitch-restraining torque would lead to a corresponding decrease in the other. Thus, penalizing one of the contributions in the objective function was sufficient to explore the power-to-load ratios. Simulations were first completed in regular waves where sample wave periods above and below the resonance frequency, with a wave amplitude of 0.02 m and maximum allowable heave displacement of 0.1 m, were presented to confirm the performance of PSC under a variety of penalty weights. When $\gamma_1 \to 0$ and $\beta_m \to 0$, the maximum PTO absorbed power was recovered with minimal reduction in system loads, but may not correspond to the location of greatest output power or power-to-load ratio. The case of $\gamma_1 \to \infty$ will lead to significantly reduced restraining loads; however, at the expense of greater PTO forces and reactive power requirements. In irregular waves, results from PSC provided an average 50% improvement in power-to-load ratio across the range of simulated peak wave frequencies, but requires the greatest reactive power of all the test cases. However, there was little growth in PTO and structural loads being comparable to or lower than the baseline absorption strategies. Furthermore, as a result of the sea spectrum spreading wave energy across multiple wave frequencies, the maximum power-to-load contours were more tightly packed than compared to regular waves. This work has highlighted some of the issues that arise when WEC control focuses solely on maximizing power absorption as it is accompanied by proportionately greater structural and PTO loads that are likely to lead to a higher levelized cost of energy. In the future, pursuit of moderate gains in TAP from control strategies may be more favorable as the increase in power absorption may outpace the growth in structural loads.

8. Acknowledgement

This work was supported by the U.S. Department of Energy under Contract No. DE-AC36-08GO28308 with the National Renewable Energy Laboratory (NREL). Funding for the work was provided by NREL's Laboratory Directed Research and Development Program. The U.S. Government retains and the publisher, by accepting the article for publication, acknowledges that the U.S. Government retains a nonexclusive, paid-up, irrevocable, worldwide license to publish or reproduce the published form of this work, or allow others to do so, for U.S. Government purposes.

Appendix A. Time-to-Frequency Domain Relations

The relations between the time- and frequency-domain radiation coefficients were derived in [35].

$$K_{r22}(t) = \frac{2}{\pi}\int_0^\infty \lambda_{22}(\sigma)\cos(\sigma t)\,d\sigma \tag{A.1}$$

$$K_{r22}(t) = -\frac{2}{\pi}\int_0^\infty \sigma\left[\mu_{22}(\sigma) - \mu_{22}(\infty)\right]\sin(\sigma t)\,d\sigma \tag{A.2}$$

where $\mu_{22}(\sigma)$ and $\lambda_{22}(\sigma)$ are the frequency-dependent hydrodynamic radiation coefficients commonly known as the added mass and wave radiation damping.

The relationship between the time- and frequency-domain excitation coefficients is given by the following equation.

$$K_{e2}(t) = \frac{1}{\pi}\int_0^\infty \left[\Re\left\{X_2(\sigma)\right\}\cos(\sigma t) - \Im\left\{X_2(\sigma)\right\}\sin(\sigma t)\right]d\sigma \tag{A.3}$$

where X_2 is the frequency-dependent, complex, wave-exciting heave-force coefficient, $\Re$ is the real component, and $\Im$ is the imaginary component.

Appendix B. Matrix Expressions

The time-derivative matrix, $\Gamma \in \mathbb{R}^{N\times N}$, is block diagonal with the following block structure.

$$\Gamma^j = \begin{bmatrix} 0 & j\sigma_0 \\ -j\sigma_0 & 0 \end{bmatrix} \text{ for } j = 1, 2, \ldots, N/2 \tag{B.1}$$

Using a change of variables, the surge-pitch radiation convolution integral can be represented in matrix form as follows.

$$f_{r12}(t) = \int_{-\infty}^{t} K_{r12}(t-\tau)\,\dot{\zeta}_2(\tau)\,d\tau = \Phi(t)\,(G_{12} - \mu_{12}(\infty)\,\Gamma)\,\hat{\psi} \tag{B.2}$$

where $G_{12} \in \mathbb{R}^{N\times N}$ is block diagonal with the following structure.

$$G_{12}^j = \begin{bmatrix} \lambda_{12}(j\sigma_0) & \sigma\mu_{12}(j\sigma_0) \\ -j\sigma_0\mu_{12}(j\sigma_0) & \lambda_{12}(j\sigma_0) \end{bmatrix} \text{ for } j = 1, 2, \ldots, N/2 \tag{B.3}$$

Appendix C. Wave-Exciting Force and Far-Field Radiated Waves

To obtain a relation between the wave-exciting force and the far-field radiated wave amplitudes (shown in Fig. 1 as $A_j^{\pm}$), we examine the fluid domain shown in Fig. C.10 [36]. In this figure, $\mathcal{B}$, $\mathcal{D}$, n, Σ_f, Σ_h, Σ_-, and Σ_+ denote the

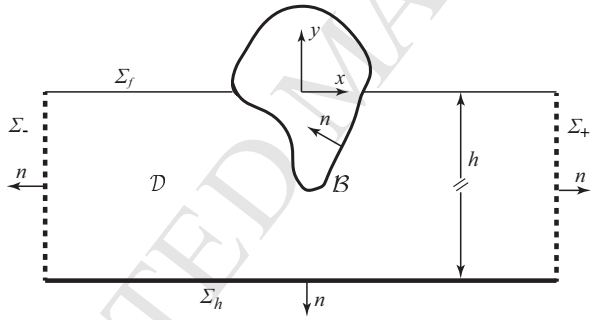

Figure C.10: Fluid domain boundaries and coordinate system.

body boundary, fluid domain, normal vector, free-surface boundary, bottom boundary, and the left and right far-field boundaries, respectively. By assuming small body motion, linearized water-wave theory, and time-harmonic flow, the velocity potential can be decomposed into incident, diffraction, and the j-th mode radiation potentials: ϕ_0, ϕ_7, and ϕ_j with $j = 1, 2, 3$ for sway, heave, and pitch, respectively. With $\zeta_j(t) = \xi_j e^{i\sigma t}$ denoting the displacement of the body in the j-th mode, the total potential can be written as follows:

$$\Phi(x, y, t) = \Re\left\{A[\phi_0(x, y) + \phi_7(x, y)]e^{i\sigma t} + \sum_{j=1}^{3} \phi_j(x, y)[i\sigma\xi_j e^{i\sigma t}]\right\} \tag{C.1}$$

The potential components ϕ_0, ϕ_7, and ϕ_j all satisfy the no-penetration boundary condition on Σ_h and the linearized free-surface boundary condition on the calm water surface Σ_f. Furthermore, the radiation potentials must satisfy the far-field radiation condition which requires outgoing waves at the far-field boundaries Σ_+ and Σ_- located at $x \to +\infty$ and $x \to -\infty$, respectively:

$$\phi_j = \frac{g}{\sigma^2}\frac{\cosh k(y+h)}{\cosh kh} A_j^{\pm} e^{\mp ikx}, \; \substack{x\to+\infty \\ x\to-\infty}, \; j = 1, 2, 3 \tag{C.2}$$

where $A_j^{\pm}$ is the far-field radiation wave amplitudes per unit body motion amplitude at Σ_+ and Σ_-. The diffraction potential ϕ_7 must also satisfy the far-field radiation condition. On the body surface, the boundary conditions for the radiation and diffraction potentials are

$$\left.\frac{\partial \phi_j}{\partial n}\right|_{\mathcal{B}} = n_j \ , \ j = 1, 2, 3 \tag{C.3}$$

and

$$\left.\frac{\partial \phi_7}{\partial n}\right|_{\mathcal{B}} = -\left.\frac{\partial \phi_0}{\partial n}\right|_{\mathcal{B}} \tag{C.4}$$

where $\mathbf{n} = (n_1, n_2)$ is the unit normal vector and $n_3 = (\mathbf{r} \times \mathbf{n})_3$ with $\mathbf{r}$ being the position vector.

For an incident wave in the form of Eq. (11), the incident potential is known and is given by

$$\phi_0 = \frac{ig}{\sigma} \frac{\cosh k(y+h)}{\cosh kh} e^{-ikx} \tag{C.5}$$

The wave-exciting force on a fixed body can be obtained from the diffraction problem [37]:

$$\begin{aligned} X_j &= -i\rho\sigma \int_{\mathcal{B}} (\phi_0 + \phi_7) n_j dS \\ &= -i\rho\sigma \int_{\mathcal{B}} (\phi_0 + \phi_7) \frac{\partial \phi_j}{\partial n} dS \ , \ j = 1, 2, 3 \end{aligned} \tag{C.6}$$

Because ϕ_j and ϕ_7 both satisfy the same free-surface, bottom, and far-field boundary conditions, Green's second identity can be applied to show that

$$X_j = -i\rho\sigma \int_{\mathcal{B}} \left(\phi_0 \frac{\partial \phi_j}{\partial n} - \phi_j \frac{\partial \phi_0}{\partial n} \right) dS \ , \ j = 1, 2, 3 \tag{C.7}$$

We have removed the unknown diffraction potential from the expression for wave-exciting force. Similarly, by taking advantage of the fact that both ϕ_0 and ϕ_j satisfy the same boundary conditions except on the body and far-field boundaries, we can apply Green's second identity again to show that

$$X_j = i\rho\sigma \int_{\Sigma_- \cup \Sigma_+} \left(\phi_0 \frac{\partial \phi_j}{\partial n} - \phi_j \frac{\partial \phi_0}{\partial n} \right) dS \ , \ j = 1, 2, 3 \tag{C.8}$$

Finally, by using Eqs. (C.2) and (C.5), the integration in Eq. (C.8) can be carried out to obtain the expression for wave-exciting force:

$$X_j = i\frac{\rho g^2}{\sigma^2} A_j^- \quad \text{as} \ \ h \to \infty \ , \ j = 1, 2, 3 \tag{C.9}$$

This relation is known as the Haskind relation for this problem, which relates the wave-exciting force to the left far-field radiated wave amplitude. Thus, with forced oscillation of the body in calm water, we can obtain the wave-exciting force on the body in the presence of incident waves. The wave-exciting force can also be related to the radiation damping of the body. For heave motion ($j = 2$), the radiation force is in the following form:

$$F_2(t) = -\mu_{22} \ddot{\zeta}_2(t) - \lambda_{22} \dot{\zeta}_2(t) \tag{C.10}$$

where μ_{22} is the heave added mass, λ_{22} is the radiation damping, and $\zeta_2(t) = \xi_2 e^{i\sigma t}$ is the heave displacement of the body. Because of the orthogonality of $\ddot{\zeta}_2(t)$ and $\dot{\zeta}_2(t)$, only the damping part of the radiation force contributes to the time averaged work done on the fluid by the body:

$$\overline{W} = \frac{1}{T} \int_0^T -F_2(t) \dot{\zeta}_2(t) \, dt = \frac{\lambda_{22} \mid \xi_2 \mid^2 \sigma^2}{2} \tag{C.11}$$

Energy flux of the linear harmonic wave, per-unit wave front, is $\overline{\dot{E}} = (1/2)\rho g A^2 V_g$, where $V_g = g/2\sigma$ in deep water. Then, the combined energy flux of radiated waves through Σ_+ and Σ_- is given in terms of the far-field radiated wave amplitudes ($A_2^{\pm}$):

$$\overline{\dot{E}} = \frac{1}{2}\rho g \mid \xi_2 \mid^2 \left(\mid A_2^+ \mid^2 + \mid A_2^- \mid^2 \right) V_g \tag{C.12}$$

By equating Eqs. (C.11) and (C.12), the relation between the radiation damping and far-field radiated wave amplitudes can be established:

$$\lambda_{22} = \frac{\rho g^2}{2\sigma^3} \left(\mid A_2^+ \mid^2 + \mid A_2^- \mid^2 \right) \tag{C.13}$$

Equations (C.9) and (C.13) together give the relation between the wave-exciting force and radiation damping:

$$\mid X_2 \mid^2 = \frac{2\rho g^2}{\sigma} \frac{\lambda_{22}}{(1+\gamma^2)} \tag{C.14}$$

where $\gamma = \mid A_2^+ / A_2^- \mid$ is the geometry-hydrodynamic radiation factor.

References

[1] F. Madhi, M. E. Sinclair, R. W. Yeung, The "Berkeley Wedge": an asymmetrical energy-capturing floating breakwater of high performance, Marine System and Technology, journal of SOBENA 9 (1) (2014) 5–16.
URL http://www.sobena.org.br/msot/downloads/MSOT_V9N1_%20paper1.pdf

[2] F. Madhi, R. W. Yeung, M. E. Sinclair, Energy-capturing floating breakwater, U.S. Patent No. 9,416,766 (August 16 2016).
URL http://patft1.uspto.gov/netacgi/nph-Parser?patentnumber=9416766

[3] N. Tom, R. W. Yeung, Performance enhancements and validations of the UC-Berkeley ocean-wave energy extractor, ASME Journal of Offshore Mechanics Arctic Engineering 135 (2) (2013) 041101. doi:10.1115/OMAE2012-83736.

[4] D. Son, V. Belissen, R. W. Yeung, Optimizing the performance of a dual coaxial–cylinder wave–energy extractor, in: Proceedings of the ASME 2015 34th International Conference on Ocean, Offshore and Arctic Engineering, no. OMAE2015-42379, St. John's, Newfoundland, Canada, 2015. doi:10.1115/OMAE2015-42379.

[5] W. Musial, M. Lawson, S. Rooney, Marine hydrokinetic technology (MHK) instrumentation, measurement, and computer modeling workshop, Tech. Rep. NREL/TP-5000-57605, National Renewable Energy Laboratory, Boulder, CO. (2013).
URL https://www.nrel.gov/docs/fy13osti/57605.pdf

[6] F. Madhi, R. W. Yeung, On survivability of asymmetric wave-energy converters in extreme waves, Renewable Energy 116 (2018) 1–19. doi:10.1016/j.renene.2017.07.123.

[7] H. Eidsmoen, Optimum control of a floating wave-energy converter with restricted amplitude, ASME Journal of Offshore Mechanics and Arctic Engineering 118 (2) (1996) 96–102. doi:10.1115/1.2828829.

[8] J. Hals, J. Falnes, T. Moan, Constrained optimal control of a heaving buoy wave-energy converter, ASME Journal of Offshore Mechanics and Arctic Engineering 133 (1) (2011) 011401. doi:10.1115/1.4001431.

[9] J. A. M. Cretel, G. Lightbody, G. P. Thomas, A. W. Lewis, Maximisation of energy capture by a wave-energy point absorber using model predictive control, in: Proceedings of the 18th World Congress of the International Federation of Automatic Control, Milano, Italy, 2011, pp. 3714–3721. doi:10.3182/20110828-6-IT-1002.03255.

[10] E. Abraham, E. C. Kerrigan, Optimal active control and optimization of a wave energy converter, IEEE Transactions on Sustainable Energy 4 (2) (2013) 324–332. doi:10.1109/TSTE.2012.2224392.

[11] G. Li, M. R. Belmont, Model predictive control of sea wave energy converters – part I: A convex approach for the case of a single device, Journal of Renewable Energy 69 (2014) 453–463. doi:10.1016/j.renene.2014.03.070.

[12] G. Bacelli, J. V. Ringwood, J. Gilloteaux, A control system for a self-reacting point absorber wave energy converter subject to constraints, in: Proceedings of the 18th World Congress of the International Federation of Automatic Control, Milano, Italy, 2011, pp. 11387–11392. doi:10.3182/20110828-6-IT-1002.03694.

[13] D. R. Herber, J. T. Allison, Wave energy extraction maximization in irregular ocean waves using pseudospectral methods, in: Proceedings of the ASME International Design Engineering Technical Conferences and Computers and Information in Engineering Conference, Portland, OR, USA, 2013. doi:10.1115/DETC2013-12600.

[14] N. M. Tom, Y. H. Yu, M. J. Lawson, A. D. Wright, Pseudo-spectral control of a novel oscillating surge wave energy converter in regular waves, part I: power optimization including load reduction, Journal of Ocean Engineering (2016) 352–366. doi:10.1016/j.oceaneng.2017.03.027.

[15] J. Falnes, Optimum control of oscillation of wave-energy converters, International Journal of Offshore and Polar Engineering 12 (2) (2002) 47–154.
URL http://folk.ntnu.no/falnes/web_arkiv/InstFysikk/optcontrl.pdf

[16] R. Genest, F. Bonnefoy, A. H. Clément, A. Babarit, Effect of non-ideal power take-off on the energy absorption of a reactively controlled one degree of freedom wave energy converter, Journal of Applied Ocean Research 48 (2014) 236–243. doi:10.1016/j.apor.2014.09.001.

[17] A. F. O. Falcão, J. C. C. Henriques, Effect of non-ideal power take-off efficiency on performance of single- and two-body reactively controlled wave energy converters, Journal of Ocean Engineering and Marine Energy (2015) 273–286. doi:10.1007/s40722-015-0023-5.

[18] A. Babarit, A. Clément, Optimal latching control of a wave energy device in regular and irregular waves, Journal of Applied Ocean Research 28 (2) (2006) 77–91. doi:10.1016/j.apor.2006.05.002.

[19] A. Babarit, M. Guglielmi, A. H. Clément, Declutching control of a wave energy converter, Journal of Ocean Engineering 36 (12) (2009) 1015–1024. doi:10.1016/j.oceaneng.2009.05.006.

[20] R. W. Yeung, A hybrid integral-equation method for time-harmonic free surface flows, in: Proceedings of the 1st International Conference on Numerical Ship Hydrodynamics, Gaithersburg, MD, 1975, pp. 58–607.

[21] W. E. Cummins, The impulse response function and ships motions, Schiffstechnik 9 (1962) 101–109.
URL http://www.marinecontrol.org/References/papers/Cummins%201962.pdf

[22] D. V. Evans, A theory for wave-power absorption by oscillating bodies, Journal of Fluid Mechanics 7 (1) (1976) 1–25. doi:10.1017/S0022112076001109.

[23] J. Hals, T. Bjarte-Larsson, J. Falnes, Optimum reactive control and control by latching of a wave-absorbing semisubmerged heaving sphere, in: Proceedings of the ASME 2002 21st International Conference on Offshore Mechanics and Arctic Engineering, no. OMAE2002-28172, Oslo, Norway, 2002. doi:10.1115/OMAE2002-28172.

[24] D. V. Evans, Maximum wave-power absorption under motion constraints, Journal of Applied Ocean Research 3 (4) (1981) 200–203. doi:10.1016/0141-1187(81)90063-8.

[25] T. Strager, P. F. López, E. V. Sánchez, et al, Optimising reactive control in non-ideal efficiency wave energy converters, in: Proceedings of the ASME 2014 33rd International Conference on Ocean, Offshore and Arctic Engineering, no. OMAE2014-23005, San Francisco, California, USA, 2014. doi:10.1115/OMAE2014-23005.

[26] G. Bacelli, J. V. Ringwood, Numerical optimal control of wave energy converters, IEEE Transactions on Sustainable Energy 6 (2) (2015) 133–145. doi:10.1109/TSTE.2014.2371536.

[27] P. Garcia-Rosa, G. Bacelli, J. V. Ringwood, Control-informed geometric optimization of wave energy converters: the impact of device motion and force constraints, Energies 8 (2015) 13672–13687. doi:10.3390/en81212386.

[28] M. S. Denis, W. J. Pierson, On the motions of ships in confused seas, in: Proceedings of the Annual Meeting of the Society of Naval Architects and Marine Engineers, New York, 1953, pp. 280–356.
URL http://www.dtic.mil/dtic/tr/fulltext/u2/045880.pdf

[29] E. Baekkedal, Alternative methods of realizing the sea spectrum for time-domain simulations of marine structures in irregular seas, Master's thesis, Norwegian University of Science and Technology, Trondheim, Norway (2014).
URL https://daim.idi.ntnu.no/masteroppgaver/011/11095/masteroppgave.pdf

[30] M. K. Ochi, Ocean Waves: The Stochastic Approach, 6, Cambridge University Press, Cambridge, UK, 2005.

[31] A. Niesłony, Determination of fragments of multiaxial service loading strongly influencing the fatigue of machine components, Journal of Renewable and Sustainable Energy 23 (8) (2009) 2712–2721. doi:10.1016/j.ymssp.2009.05.010.

[32] H. J. Sutherland, On the fatigue analysis of wind turbines, Tech. Rep. SAND99-0089, Sandia National Laboratories (1999). doi:10.2172/9460.

[33] P. Ragan, L. Manuel, Comparing estimates of wind turbine fatigue loads using time-domain and spectral methods, Wind Engineering 31 (2) (2007) 83–99. doi:10.1260/030952407781494494.

[34] N. M. Tom, Y. H. Yu, A. D. Wright, M. J. Lawson, Balancing power absorption against structural loads with viscous drag and power-take-off efficiency considerations, IEEE Journal of Oceanic Engineering (2017) (Accepted for Publication).

[35] T. F. Ogilvie, Recent progress towards the understanding and prediction of ship motions, in: Proceedings of the Fifth Symposium on Naval Hydrodynamics, Bergen, Norway, 1964, pp. 3–79.
URL http://mararchief.tudelft.nl/catalogue/entries/12149/

[36] R. W. Yeung, J. V. Wehausen, W. C. Webster, Hydrodynamics of ships and ocean systems - II, Lectures notes for the course NAOE-241b, University of California at Berkeley (1983).

[37] J. N. Newman, The exciting forces on fixed bodies in waves, Tech. rep., Dept. of the Navy, David Taylor Model Basin in Washington, D.C. (1963).
URL http://hdl.handle.net/1721.3/49043

NREL
NATIONAL RENEWABLE ENERGY LABORATORY

Journal of Renewable Energy

Power-to-Load Balancing for Asymmetric Heave Wave Energy Converters with Nonideal Power-Take-Off

Highlights

- Review of "The Berkeley Wedge" an asymmetric wave energy converter/breakwater device
- Includes effect of power-take-off efficiency and force coefficients on power output
- Use of pseudo-spectral control theory while including structural and actuator loads
- Introduces a power-to-load ratio for evaluating wave energy converter performance
- Losses in power capture were exceeded by reductions in structural and actuator loads

15013 Denver West Parkway
Golden, CO 80401
Phone 303-275-3000

NREL is a national laboratory of the U.S. Department of Energy
Office of Energy Efficiency & Renewable Energy
Operated by the Alliance for Sustainable Energy, LLC